The Astrophysical Journal, 876:112 (18pp), 2019 May 10 https://doi.org/10.3847/1538-4357/ab0e0f

Strong Far-ultraviolet Fields Drive the [C II]/Far-infrared Deficit in $z \sim 3$ Dusty, Star-forming Galaxies

Matus Rybak[1], G. Calistro Rivera[1], J. A. Hodge[1], Ian Smail[2], F. Walter[3], P. van der Werf[1], E. da Cunha[4], Chian-Chou Chen[5], H. Dannerbauer[6], R. J. Ivison[5,7], A. Karim[8], J. M. Simpson[9], A. M. Swinbank[2], and J. L. Wardlow[10]

[1] Leiden Observatory, Leiden University, P.O. Box 9513, NL-2300 RA Leiden, The Netherlands; mrybak@strw.leidenuniv.nl
[2] Centre for Extragalactic Astronomy, Department of Physics, Durham University, South Road, Durham DH1 3LE, UK
[3] Max Planck Institute for Astronomy, Königstuhl 17, D-69117 Heidelberg, Germany
[4] The Australian National University, Mt. Stromlo Observatory, Cotter Road, Weston Creek, ACT 2611, Australia
[5] European Southern Observatory, Karl-Schwarzschild-Strasse 2, D-85748 Garching bei München, Germany
[6] Dpto. Astrofísica, Universidad de La Laguna, E-38206 La Laguna, Tenerife, Spain
[7] Institute of Astronomy, University of Edinburgh, Royal Observatory, Blackford Hill, Edinburgh EH9 3HJ, UK
[8] Max-Planck-Institut für Radioastronomie, Auf dem Hügel 69, D-53121 Bonn, Germany
[9] Academia Sinica Institute of Astronomy and Astrophysics, No. 1, Sec. 4, Roosevelt Road, Taipei 10617, Taiwan
[10] Physics Department, Lancaster University, Bailrigg, Lancaster LA1 4YB, UK
Received 2018 October 6; revised 2019 January 28; accepted 2019 March 5; published 2019 May 8

Abstract

We present 0.″15 (1 kpc) resolution ALMA observations of the [C II] 157.74 μm line and rest-frame 160 μm continuum emission in two $z \sim 3$ dusty, star-forming galaxies—ALESS 49.1 and ALESS 57.1, combined with resolved CO (3–2) observations. In both sources, the [C II] surface brightness distribution is dominated by a compact core $\leqslant$1 kpc in radius, a factor of 2–3 smaller than the extent of the CO (3–2) emission. In ALESS 49.1, we find an additional extended (8 kpc radius), low surface brightness [C II] component. Based on an analysis of mock ALMA observations, the [C II] and 160 μm continuum surface brightness distributions are inconsistent with a single-Gaussian surface brightness distribution with the same size as the CO (3–2) emission. The [C II] rotation curves flatten at $\simeq$2 kpc radius, suggesting that the kinematics of the central regions are dominated by a baryonic disk. Both galaxies exhibit a strong [C II]/far-IR (FIR) deficit on 1 kpc scales, with FIR surface brightness to [C II]/FIR slope steeper than in local star-forming galaxies. A comparison of the [C II]/CO (3–2) observations with photodissociation region models suggests a strong far-UV (FUV) radiation field ($G_0 \sim 10^4$) and high gas density (n(H) $\sim 10^4$–10^5 cm^{-3}) in the central regions of ALESS 49.1 and ALESS 57.1. The most direct interpretation of the pronounced [C II]/FIR deficit is a thermal saturation of the C^+ fine-structure levels at temperatures $\geqslant$500 K, driven by the strong FUV field.

Key words: galaxies: high-redshift – galaxies: star formation – submillimeter: galaxies

Supporting material: data behind figure

1. Introduction

Dusty, star-forming, submillimeter galaxies (DSFGs, SMGs) are a major contributor to the global star formation rate (SFR) between redshifts $z = 2$ and 4, at an epoch when the star-forming activity of the universe was at its peak (e.g., Casey et al. 2014). Although few in number, thanks to their high SFRs (>100 $M_\odot$ yr^{-1}), up to 20% of all the star formation at $z \sim 3$ takes place in SMGs (Swinbank et al. 2014).

The massive dust reservoirs in SMGs absorb the UV/optical radiation from the newborn stars, mostly reradiating it thermally as a rest-frame far-IR (FIR)/submillimeter continuum.[11] Therefore, studying the structure and physical properties in these extreme sources requires relying on submillimeter/millimeter-bright tracers—the dust continuum (which directly traces the obscured star formation) and low-J CO rotational transitions[12] (which trace the cold, molecular gas that fuels the star formation; Carilli & Walter 2013).

Besides the FIR continuum and CO emission, the third bright rest-frame FIR tracer of the star-forming interstellar medium (ISM) is the [C II] 157.74 μm line, a fine-structure transition of C^+ ions. Due to its low ionization energy (11.3 eV) and a relatively low critical density, [C II] traces a wide range of ISM phases—from the ionized H II regions to warm molecular clouds to diffuse gas. Depending on the environmental conditions, the upper fine-structure level is populated predominantly by collisions with H, H_2, or electrons (Goldsmith et al. 2012).

Starting in the early 1990s, systematic studies of [C II] emission in local galaxies were enabled by the *Infrared Space Observatory* and the Kuiper Airborne Observatory. These observations revealed a tight correlation between the [C II] line and FIR continuum emission from the heated dust at low SFR surface densities (e.g., Stacey et al. 1991). However, this correlation breaks at larger FIR surface brightness $\Sigma_{\rm FIR}$—the so-called "[C II]/FIR deficit" (e.g., Malhotra et al. 1997, 2001; Luhman et al. 1998, 2003)—with the [C II]/FIR ratio decreasing with increasing $\Sigma_{\rm FIR}$.

In the past decade, the study of [C II] emission in the nearby universe has been revolutionized by *Herschel*. The largest sample of [C II] observations in nearby starburst galaxies was presented by Díaz-Santos et al. (2013), who obtained PACS spectroscopic observations of the 241 galaxies from the Great

[11] Following Casey et al. (2014), we consider SMGs to comprise high-redshift galaxies with a continuum flux $\geqslant$1 mJy between 250 μm and 2 mm.
[12] In this work, we use the term "low-J" transitions for the rotational transitions with $J_{\rm upp} \leqslant 3$.

Observatories All-sky LIRG Survey (GOALS; Armus et al. 2009). Further systematic studies of the [C II] emission in local galaxies have confirmed strong correlation of the [C II]/FIR deficit with $\Sigma_{\rm SFR}$ down to 200 pc scales, in a wide range of environments from normal galaxies (Smith et al. 2017; Herrera-Camus et al. 2018) to starbursts (Díaz-Santos et al. 2017) and active galactic nucleus (AGN) hosts (Herrera-Camus et al. 2018).

At the highest redshifts ($z > 4$), the importance of the [C II] line increases dramatically, as the raised cosmic microwave background temperature renders the low-J CO emission undetectable, while the [C II] line remains relatively unaffected (da Cunha et al. 2013; Vallini et al. 2015; Lagache et al. 2018). Indeed, with the advent of the Atacama Large Millimeter/submillimeter Array (ALMA), [C II] observations are now increasingly used to determine redshifts and dynamical masses of high-redshift galaxies, including some of the most distant systems (Walter et al. 2009; Brisbin et al. 2015; Gullberg et al. 2015; Oteo et al. 2016; Carniani et al. 2017; Decarli et al. 2018; Smit et al. 2018). Most recently, Gullberg et al. (2018) presented deep, 30 mas resolution (200 pc physical scale) ALMA observations of the [C II] line in four (unlensed) $z = 4.4$–4.8 galaxies. Although their observation suffered from a very sparse u-v plane coverage, they found the resolved [C II]/FIR deficit at $z \sim 4.5$ to follow the trend seen in local galaxies. Similarly, high-resolution ALMA observations of the [C II]/FIR deficit in two strongly lensed galaxies at $z = 1.7$ and 5.6 were recently presented by Lamarche et al. (2018) and Litke et al. (2019), respectively, showing a pronounced [C II]/FIR deficit (10^{-4} to 10^{-3}) on (sub)kiloparsec scales.

Despite the recent progress, it is still unclear how well the results and relations derived from local observations hold for the high-redshift population, especially the intensely star-forming high-redshift SMGs, with $\Sigma_{\rm SFR}$ two to three orders of magnitude higher than the local star-forming galaxies (10^{-3} to 1 $M_\odot\,{\rm yr}^{-1}\,{\rm kpc}^{-2}$; e.g., Smith et al. 2017). To directly compare the [C II] emission in high-redshift SMGs to the local galaxies and study its connection to the star formation, high-resolution (kiloparsec-scale) observations of the [C II] emission, alongside the rest-frame FIR continuum (tracing the obscured star formation) and the low-J CO emission tracing the molecular gas, are necessary.

At high redshift, such resolved, multitracer studies are limited by the angular extent of the source (few arcseconds at most) and the need for robust redshifts to ensure that both [C II] and low-J CO emission are observable from the ground. For example, Stacey et al. (2010) compared unresolved [C II]/FIR/CO ($J_{\rm upp} \leqslant 4$) observations of a heterogeneous sample of $z = 1$–2 galaxies. Gullberg et al. (2015) compared [C II], FIR, and CO (2–1)/CO (1–0) observations in 20 strongly lensed SMGs ($z_{\rm source} = 2.1$–5.7); they found the [C II] and CO line profiles to be very similar, suggesting that they originate from the same source-plane regions. However, the limited spatial resolution of these observations prevented a robust source-plane reconstruction of the CO/[C II] emission; the *differential magnification* bias (e.g., Serjeant 2012) therefore could not be eliminated. In addition, several individual sources at $z > 4.5$ have been studied in both [C II] and low-J CO emission (e.g., Walter et al. 2009; Huynh et al. 2014; Cicone et al. 2015), though these tend to be extreme sources in terms of FIR brightness and AGN activity.

Finally, the [C II] line has been proposed as an alternative to CO emission as a molecular gas tracer (e.g., Zanella et al. 2018). However, in SMGs, the spatial extent of CO emission has been shown to vary strongly with $J_{\rm upp}$ (e.g., Ivison et al. 2011; Riechers et al. 2011). If [C II] emission traces only a subset of the molecular gas reservoir, [C II]-based mass estimates might be severely biased.

In this paper, we explore a new regime in resolved, multitracer studies by investigating resolved [C II], FIR continuum, and CO (3–2) emission on kiloparsec scales in two (unlensed) $z \sim 3$ sources. This allows us to address the following questions:

1. How does the resolved [C II]/FIR ratio at $z \sim 3$ compare to that seen in local and high-redshift star-forming galaxies?
2. What physical mechanism drives the [C II]/FIR deficit in SMGs?
3. How well does the [C II] emission trace the molecular gas reservoir in SMGs?

Compared to the high-redshift, high-resolution [C II]-only studies (e.g., Gullberg et al. 2018; Zanella et al. 2018), resolved emission-line maps of two different species (C^+ and ^{12}CO) allow us to study the relation between [C II] emission and the colder molecular gas.

This paper is structured as follows. In Section 2, we give the details of ALMA observations. Section 3 details the processing of the data in both the image plane and u-v plane, the assessment of the systematic errors, and kinematic modeling. Section 4 presents the spatial and kinematic comparison of the interpretation of the [C II]/CO (3–2)/FIR observations, results of photodissociation region (PDR) modeling, and a discussion of the physical processes driving the [C II]/FIR deficit. Finally, Section 5 summarizes the conclusions of this paper.

Throughout this paper we use a flat ΛCDM cosmology from Planck Collaboration et al. (2016). We adopt the CO (3–2) spectroscopic redshifts from Calistro Rivera et al. (2018): $z = 2.943$ and $z = 2.943$ for ALESS 49.1 and ALESS 57.1, respectively. Consequently, 1 arcsec corresponds to 7.9 kpc for both ALESS 49.1 and ALESS 57.1; the luminosity distance to both sources is 25,445 Mpc (Wright 2006).

2. Observations and Data Reduction

2.1. Sample Selection

The two galaxies analyzed in this paper were identified by Hodge et al. (2013) as a part of the ALESS survey. The ALESS survey was an ALMA Cycle 0 870 μm imaging campaign targeting all 126 sources discovered in the LABOCA Extended *Chandra* Deep Field South Submillimeter Survey (LESS; Weiß et al. 2009). With ALMA Cycle 0 observations providing a significant improvement over the LABOCA map in both resolution (beam area reduced by a factor of ∼200) and sensitivity (increased by a factor of ∼3), the ALESS survey identified 99 distinct submillimeter-bright galaxies in its primary sample (Hodge et al. 2013). Out of these, at the time of the proposal (2015 April) only four—ALESS 49.1, ALESS 57.1, ALESS 67.1, and ALESS 122.1—had robust redshifts that allowed for ALMA observations of both the low-J CO and [C II] lines. The spectroscopic redshifts were acquired using

Table 1
Source Positions (Corresponding to the 160 μm Continuum Surface Brightness Maximum), Redshifts, ALMA Band 8 Naturally Weighted Beam Sizes and Noise Levels, Observed 160 μm Continuum/[C II] Flux Densities, and the FWHM of the [C II] and CO (3–2) Lines

Source		ALESS 49.1	ALESS 57.1
R.A. (J2000)		3:31:24.71	3:31:51.94
Decl. (J2000)		−27:50:46.9	−27:53:27.0
z[a]		2.943 ± 0.001	2.943 ± 0.002
Beam FWHM	(arcsec)	0.16 × 0.12	0.16 × 0.12
Beam PA	(deg)	53	56
$S_{160\,\mu m}$	(mJy)	10.7 ± 1.0	8.2 ± 0.5
$I^{max}_{160\,\mu m}$	(mJy beam^{-1})	3.42 ± 0.16	1.53 ± 0.17
$S_{[C\,II]}$[a]	(mJy)	15.4 ± 2.8	8.8 ± 2.5
$I^{max}_{[C\,II]}$[b]	(mJy beam^{-1})	2.0 ± 0.4	3.0 ± 0.4
FWHM$_{[C\,II]}$	(km s^{-1})	600 ± 130	390 ± 70
FWHM$_{CO}$[a]	(km s^{-1})	610 ± 30	360 ± 90

Notes. The redshifts are based on CO (3–2) observations (Calistro Rivera et al. 2018). The spatially integrated 160 μm and [C II] flux densities are measured within a circular aperture with a 1.″0 diameter, centered on the continuum surface brightness maximum.
[a] Adopted from Calistro Rivera et al. (2018).
[b] Integrated over 800 and 710 km s^{-1} for ALESS 49.1 and ALESS 57.1, respectively.

VLT-FORS2/VIMOS and Keck-DEIMOS and are based on multiple line detections (Danielson et al. 2017).

In this paper, we present the ALMA Band 8 observations targeting the [C II] line and rest-frame 160 μm continuum. The corresponding Band 3 observations, targeting the CO (3–2) (ν_{rest} = 345.795 GHz) emission, were recently presented by Calistro Rivera et al. (2018).

2.2. ALMA Band 8 Observations

The observations were carried out as part of the ALMA Cycle 3 Project #2015.1.00019.S (PI: J. Hodge) on 2016 August 12. Only ALESS 49.1 and ALESS 57.1 ([C II] line in ALMA Band 8) were observed; ALESS 67.1 (z = 2.12) and ALESS 122.1 (z = 2.02) have the [C II] line in ALMA Band 9 and were not observed. The total time including calibration and overheads was 72 minutes, with an on-source time of 11 minutes per target. The array configuration consisted of 38 12 m antennas, with baselines extending up to 1400 m. The largest angular scale[13] of the observations is ∼1.″9 for both sources. The primary beam FWHM is 14.″1. Synthesized beam sizes and σ_{rms} for the 160 μm continuum and the [C II] emission are listed in Table 1. The target elevation range was 66°–73° for ALESS 49.1 and 67°–76° for ALESS 57.1.

The frequency setup was configured in four spectral windows (SPWs) in Band 8. The individual SPWs were centered at 481.953, 483.183, 493.506, and 495.386 GHz. Each SPW was split into 480 frequency channels 3.906 MHz wide, giving a total bandwidth of 1.875 GHz per SPW. The radio-velocity resolution was 2.42 km s^{-1}. Both the Stokes *XX* and *YY* parameters were observed.

The data were calibrated using the standard ALMA pipeline, with additional flagging necessary to remove atmospheric features (see Section 3.1). All the visibility data processing apart from imaging was performed using CASA versions 4.7 and 5.0 (McMullin et al. 2007).

The spectral structure of the [C II] line overlaps with atmospheric absorption features at 481.2 and 481.6 GHz. Consequently, the noise level in the affected channels is raised by a factor of ∼2. This issue is particularly severe for ALESS 49.1. Another atmospheric feature is located in a line-free SPW at 496.35 GHz; here the affected channels were flagged to improve the continuum signal-to-noise ratio (S/N). As will be outlined in Section 3.1, we use a channel-dependent threshold for the deconvolution process to avoid introducing noise features from the affected channels.

To increase the S/N, each line was split into frequency bins ∼120 km s^{-1} wide. Additionally, we time-averaged the data using a 30 s bin; this corresponds to an average intensity loss of <0.5% at 5 arcsec from the phase-tracking center, which we consider negligible.[14] The time-bin size was chosen so as to prevent significant time-averaging smearing. The two linear polarizations were combined into the Stokes intensity *I*.

2.3. ALMA Band 3 Observations

ALMA Band 3 observations of the CO (3–2) and rest-frame 1.0 mm continuum in ALESS 49.1 and ALESS 57.1 were presented by Calistro Rivera et al. (2018). These consisted of Cycle 2 observations of ALESS 49.1 and ALESS 57.1 (Project #2013.1.00470.S; PI: J. Hodge) at 0.34–0.″67 resolution and additional Cycle 4 observations of ALESS 49.1 (Project #2016.1.00754.S; PI: J. Wardlow) at 1.″1 resolution. The naturally weighted Band 3 synthesized beam size is 0.69 × 0.″63 for ALESS 49.1 (after concatenating the Cycles 2 and 4 data) and 0.67 × 0.″60 for ALESS 57.1, with a continuum σ_{rms} of 17.6 and 19.5 μJy beam^{-1}, respectively. For a detailed description of the data and the resulting analysis, we refer the reader to Calistro Rivera et al. (2018).

3. Results

3.1. Image Analysis

3.1.1. Imaging

We perform synthesis imaging of the visibility data using the WS-CLEAN algorithm introduced by Offringa et al. (2014), specifically its multiscale version (Offringa & Smirnov 2017). The multiscale WS-CLEAN is an advanced deconvolution algorithm with a multiscale, multifrequency capability (Offringa & Smirnov 2017). Another advantage of the WS-CLEAN as opposed to the CASA implementation is the channel-dependent deconvolution threshold. As the noise level changes appreciably with frequency owing to atmospheric lines, this prevents us from introducing noise peaks from the affected channels into the reconstructed images.

For the line imaging, we first subtract the continuum by linearly interpolating the line-free channels in SPWs 1, 2, and 3 and subtract the continuum slope from the line-containing channels. The continuum channels overlapping with the atmospheric lines were flagged before the continuum subtraction. For the continuum imaging, we discard the entire SPW 0 and the line-containing channels in SPW1, as well as the channels affected by the atmospheric feature around 496.35 GHz.

[13] The largest angular scale is estimated as $0.983/\lambda_{5\%}$, where $\lambda_{5\%}$ is the 5th percentile *u-v* distance (ALMA Cycle 5 Technical Handbook).

[14] See Taylor et al. (1999), Chapter 18, Equation (42).

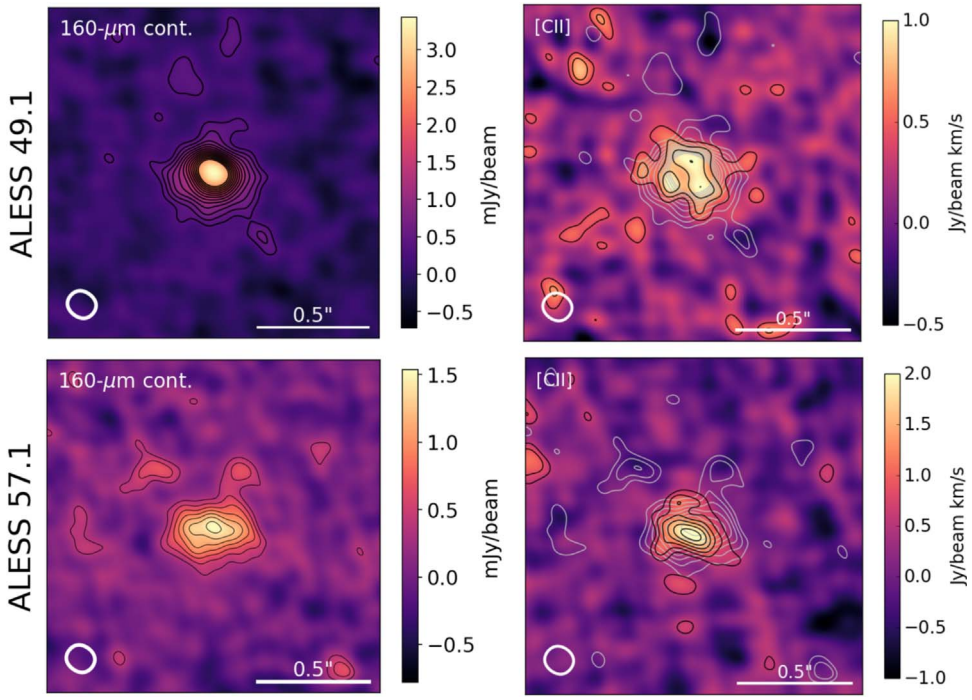

Figure 1. ALESS 49.1 and ALESS 57.1 imaging: continuum (right) and integrated [C II] emission (left) maps with continuum contours overplotted in gray. The contours start at the 2σ level and increase by 1σ. The FWHM beam size is indicated by the ellipse in the lower left corner. The [C II] and 160 μm emission is well resolved in both sources and almost cospatial.

The data were deconvolved on a sky-plane grid of 1024×1024 5 mas pixels (total field of view [FOV] size $= 5.115 \times 5.''115$), using natural weighting. We use the automatic S/N-based masking, with `an auto-mask` S/N threshold of 2.

For consistency, we reimage the CO (3–2) data of Calistro Rivera et al. (2018) using the exactly same procedure as for the [C II] data; these result in minor ($\leqslant$10%) changes in the rms noise and the inferred CO (3–2) luminosity. We use these reimaged data only for the spectral comparison in Section 4; the CO (3–2) source size and hence the bulk of our analysis in Section 4 are based on the *u-v* plane analysis and hence are unaffected by the imaging procedure. We adopt Calistro Rivera et al. (2018) CO (3–2) luminosity and gas mass estimates for the remainder of this paper.

3.1.2. ALMA 160 μm Continuum

The rest-frame 160 μm continuum is detected in both sources at $>10\sigma$ confidence (Figure 1). In both sources, the continuum emission shows only a single brightness peak at $0.''15$ resolution. In ALESS 49.1, the continuum emission is almost circularly symmetric, with a minor extension in the east–west direction. In ALESS 57.1, the continuum is noticeably extended in the east–west direction (axis ratio $\sim$ 2:1). The spatially integrated 160 μm continuum flux density for ALESS 49.1 and ALESS 57.1 is given in Table 1. The 160 μm flux density is calculated from an aperture with a $1.''0$ diameter, centered on the 160 μm continuum surface brightness maximum. The aperture size was chosen based on the FIR continuum and [C I] sizes determined from the *u-v* plane fitting (Section 3.2), as we do not expect a significant surface brightness contribution $\geqslant 0.''5$ from the center of the source.

3.1.3. [C II] Emission

The velocity-integrated maps of the [C II] emission are presented in Figure 1. The [C II] emission is detected at 5σ and 8σ significance in ALESS 49.1 and ALESS 57.1, respectively. The [C II] emission is relatively compact ($<0.''5$ diameter) in both ALESS 49.1 and ALESS 57.1, similar in extent to the 160 μm continuum. The [C II] emission in ALESS 57.1 is highly elliptical (axis ratio $\geqslant$ 2:1) and elongated in the east–west direction; the [C II] does not show any significant offset from the 160 μm peak. Note that the low-significance clumpy substructure, such as that seen in ALESS 49.1 [C II] maps, is often an artifact of low S/N (e.g., Hodge et al. 2016; Gullberg et al. 2018), rather than a real physical feature.

3.2. u-v Plane Analysis

We estimate the size of the continuum and [C II] emission regions by directly fitting the observed visibility function. Given the relatively low S/N of the data, we assume the surface brightness distribution to follow a circularly symmetric Gaussian profile.

The size is measured using the spectrally averaged continuum and line data sets. To correct the offset between the phase-tracking center and the centroid of the surface brightness distribution given in Table 1, each data set is phase-shifted to center the FOV on the centroid of the source. The data are then radially binned into bins of equal width. To test the robustness of the *u-v* plane fitting against the *u-v* bin size, we vary the *u-v* bin size from 5 to 50 kλ.

We fit each *u-v* plane data set with (1) a single Gaussian profile; (2) two Gaussian components to investigate the possibility of having compact, bright [C II] emission embedded in an extended, low surface brightness component; and (3) a combination of a single-Gaussian profile and a constant term,

corresponding to a point source in the image plane. To determine whether the two-component model significantly improves the goodness of fit compared to the one-component model, we compare the two models using the F-test (Bevington & Robinson 2003). The single-component model is preferred for the continuum emission in ALESS 49.1 and [C II] emission in ALESS 57.1, independently of the u-v bin size. We will address the robustness of the inferred $R_{1/2}$ in Section 3.2.1. The two-component model is strongly ($p > 0.95$) preferred for the [C II] emission in ALESS 49.1 and the continuum emission in ALESS 57.1. We do not find the Gaussian + constant-term (point-source) model to be preferred over the single-Gaussian model for any data set considered. The best-fitting values for the two-component model are listed in Table 2. Figure 2 shows the visibility function for the [C II] and 160 μm continuum, as well as the CO (3–2) observations from Calistro Rivera et al. (2018) and the corresponding best-fitting profiles.

In physical units, for the single-Gaussian models, the [C II] and 160 μm emission is rather compact ($R_{1/2} = 0.8$–1.4 kpc) in both sources. The [C II] and 160 μm continuum sizes from the single-Gaussian fitting agree within 1σ–2σ uncertainty. For the two-Gaussian models, the compact and extended [C II] components in ALESS 49.1 have half-light radii of 1.01 ± 0.12 kpc and 8.7 ± 1.6 kpc, respectively. The compact and extended 160 μm components in ALESS 57.1 have half-light radii of 0.86 ± 0.07 kpc and 5.3 ± 1 kpc, respectively.

For the two-component [C II] model in ALESS 49.1, the extended [C II] component accounts for up to 80% of the total [C II] luminosity. Note that the systematic uncertainty on this estimate might be significant, as it is unclear how much the extended component departs from the assumption of a circular Gaussian profile. For the [C II] emission in ALESS 57.1, the single-Gaussian model is preferred. However, if we speculate that ALESS 57.1 has an extended [C II] component with the same size as in ALESS 49.1 ($R_{1/2}^{\rm ext} = 1\farcs01$), the 3σ upper limit on the total flux density contributed by this hypothetical component is 80%. Similarly, if we speculate that the 160 μm continuum in ALESS 49.1 has an extended component identical in size to that in ALESS 57.1 ($R_{1/2}^{\rm ext} = 0\farcs67$), the 3σ upper limit on the flux contained in this hypothetical component is 50%.

How will the extended components in ALESS 49.1 [C II] emission and ALESS 57.1 160 μm continuum contribute to the observed [C II]/160 μm surface brightness distribution? The half-light radius of the ALESS 57.1 160 μm extended component is well below the maximum recoverable scale ($1\farcs9$) and therefore should be fully accounted for in the synthesized images. This is supported by the results from the spectral energy distribution (SED) modeling (Section 3.4), which indicate that the 160 μm continuum is not significantly resolved out. For the [C II] emission, the half-light radius of the extended component in ALESS 49.1 is comparable to the maximum recoverable scale, and some emission is likely resolved out in the synthesized images. However, while the extended [C II] component in ALESS 49.1 dominates the total [C II] luminosity, it contributes only between 5% and 20% of the surface brightness across the inner $R < 2$ kpc region. It is for this reason that our analysis in Sections 4.2–4.4 focuses on the central regions ($R \leqslant 2$ kpc) of ALESS 49.1 and ALESS 57.1, including the uncertainty from the extended components in further analysis.

Table 2
Inferred Source Properties for ALESS 49.1 and ALESS 57.1

Source		ALESS 49.1	ALESS 57.1
SED Fitting			
$L_{3-2000\,\mu m}$	($10^{12}\,L_\odot$)	$7.1^{+0.8}_{-0.9}$	$7.4^{+0.9}_{-0.9}$
SFR	($M_\odot\,{\rm yr}^{-1}$)	490^{+30}_{-60}	480^{+70}_{-60}
$T_{\rm dust}$	(K)	46^{+6}_{-2}	51^{+7}_{-4}
$M_\star$	($10^{10}\,M_\odot$)	$4.4^{+1.8}_{-0.3}$	$4.3^{+1.7}_{-0.8}$
$M_{\rm gas}$ [a]	($10^{10}\,M_\odot$)	5 ± 2	5 ± 2
$M_{\rm dust}$	($10^{8}\,M_\odot$)	$4.4^{+0.5}_{-0.7}$	$4.1^{+0.5}_{-0.6}$
Line Luminosities			
$L_{\rm [C\,II]}$	($10^{9}\,L_\odot$)	3.0 ± 0.8	1.1 ± 0.4
$L'_{\rm [C\,II]}$	(10^{10} K km s^{-1} pc^2)	14 ± 4	5.1 ± 1.7
$L_{\rm CO(3-2)}$ [b]	($10^{9}\,L_\odot$)	0.070 ± 0.005	0.062 ± 0.016
$L'_{\rm CO(3-2)}$ [b]	(10^{11} K km s^{-1} pc^2)	0.51 ± 0.04	0.05 ± 0.01
$L_{\rm CO(1-0)}$ [b]	($10^{6}\,L_\odot$)	2.1 ± 0.2	2.6 ± 0.7
Source sizes—Single Gaussian			
$R_{1/2}^{\rm [C\,II]}$	(arcsec)	0.163 ± 0.013	0.101 ± 0.010
$S^{\rm [C\,II]}$	(mJy)	10.9 ± 0.9	8.6 ± 0.9
$R_{1/2}^{160\,\mu m}$	(arcsec)	0.173 ± 0.009	0.128 ± 0.006
$S^{160\,\mu m}$	(mJy)	11.2 ± 0.4	7.6 ± 0.4
$R_{1/2}^{\rm CO}$ [b]	(arcsec)	0.33 ± 0.5	0.39 ± 0.06
Source sizes—Two Gaussians			
$R_{1/2}^{\rm [C\,II]}$ (compact)	(arcsec)	0.128 ± 0.015	⋯
$R_{1/2}^{\rm [C\,II]}$ (extended)	(arcsec)	1.1 ± 0.3	⋯
$S^{\rm [C\,II]}$ (compact)	(mJy)	7.4 ± 1.1	⋯
$S^{\rm [C\,II]}$ (extended)	(mJy)	29 ± 8	⋯
$R_{1/2}^{160\,\mu m}$ (compact)	(arcsec)	⋯	0.109 ± 0.007
$R_{1/2}^{160\,\mu m}$ (extended)	(arcsec)	⋯	0.67 ± 0.11
$S^{160\,\mu m}$ (compact)	(mJy)	⋯	5.8 ± 0.5
$S^{160\,\mu m}$ (extended)	(mJy)	⋯	7.6 ± 1.4
[C II] and CO (3–2) Kinematics			
$i_{\rm [C\,II]}$	(deg)	39 ± 5	58 ± 5
$M_{\rm dyn}^{\rm [C\,II]}$ ($R \leqslant 2$ kpc)	($10^{10}\,M_\odot$)	6.2 ± 5.5	2.7 ± 1.6
$M_{\rm dyn}^{\rm CO}(R < R_{1/2}^{\rm CO})$	($10^{10} M_\odot$)	11 ± 2	11 ± 5

Notes. For the global source properties derived from the SED fitting (Section 3.4), we provide the median value of the posterior probability density function. The [C II] and CO (3–2) line luminosities are spectrally integrated over the full extent of the [C II], rather than over FWHM only (as in Calistro Rivera et al. 2018), as the [C II] line exhibits a non-Gaussian profile. The source sizes are inferred from the u-v plane fitting (Section 3.2); we list the best-fitting one-component Gaussian model parameters, as well as the two-component Gaussian models if preferred by evidence. The source inclinations and [C II]-based dynamical masses are inferred from the GALPAK3D modeling (Section 3.3).

[a] Calistro Rivera et al. (2018). $M_{\rm gas}$ estimated assuming $\alpha_{\rm CO} = 1.0$.

[b] Calistro Rivera et al. (2018). $L_{\rm line}$ integrated over the entire line width as opposed to integrating only over FWHM as in Calistro Rivera et al. (2018).

3.2.1. How Robust Are the Source Sizes Determined from the u-v Plane Fitting?

Before analyzing our resolved [C II] and 160 μm continuum observations, we assess the reliability of the inferred source sizes. In particular, we investigate a possibility that the [C II]/

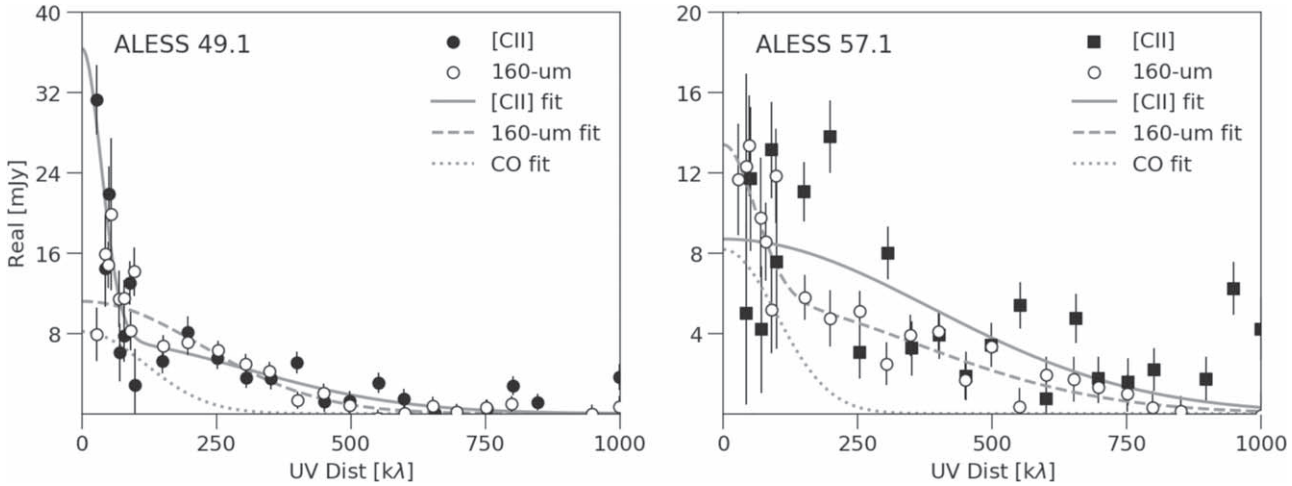

Figure 2. Azimuthally averaged visibility function for ALESS 49.1 (left) and ALESS 57.1 (right), for the [C II] and 160 μm continuum with best-fitting model (solid and dashed lines) and best-fitting single-Gaussian profiles to the CO (3–2) data (dotted line, increased by a factor of 10; Calistro Rivera et al. 2018). For added clarity, the data are binned with a 10–50 kλ bin size and truncated at 1000 kλ. In ALESS 49.1, the excess [C II] flux at short baselines—corresponding to the extended component—is clearly visible.

160 μm emissions follow CO (3–2) surface distribution and that the source sizes inferred in Section 3.2 are an artifact of the limited short-spacing coverage of our Band 8 observations. We estimate this uncertainty using simulated ALMA observations.

The mock observations are created as follows. First, we calculate the mean and rms scatter for the [C II] and 160 μm continuum visibilities within a given u-v bin. We then subtract the mean signal from the data, which gives us a u-v plane coverage corresponding exactly to a given observation, along with a realistic noise measurement for each baseline. We choose this approach to account for the different noise levels for each data set and the effect of the atmospheric lines on our [C II] data. We then inject an artificial source into the data, generating 1000 data sets with different noise realizations for each source. We consider sources with a half-light radius of 0.1–1.″0 and peak surface brightness of 0.05–4.0 mJy beam^{-1}. Finally, we bin the mock visibilities in the u-v plane using exactly the same procedure as applied to real data in Section 3.2.

Figure 3 shows the inferred radius as a function of the surface brightness maximum alongside the 1σ uncertainty from the u-v plane fitting. The measured [C II] and 160 μm continuum sizes in ALESS 49.1 and ALESS 57.1 are all smaller than sizes inferred for input sources with $R_{1/2} \geqslant 0.''2$ in the relevant peak surface brightness range. In other words, given the observed peak surface brightness, $R_{1/2}^{[\mathrm{C\,II}]} > 0.2$ arcsec source sizes would be recovered within 10% uncertainty for both ALESS 49.1 and ALESS 57.1. For comparison, the CO (3–2) half-light radii in ALESS 49.1 and ALESS 57.1 are $R_{1/2}^{\mathrm{CO}} = 0.33 \pm 0.06$ arcsec and $0.39 \pm 0.''06$, respectively.

Therefore, we consider it unlikely that the [C II]/160 μm continuum follow a single-Gaussian surface brightness distribution with the same size as CO (3–2) emission ($0.33 \pm 0.''05$ and $0.39 \pm 0.''06$ for ALESS 49.1 and ALESS 57.1, respectively). However, we cannot exclude a combination of a bright compact and faint extended [C II] and continuum components. In the following analysis, we will focus on the center of the sources where the extended [C II] component is not expected to contribute significantly.

3.3. [C II] Spectra and Kinematics

Figure 4 presents the [C II] moment-1 (intensity-weighted velocity) maps and the comparison of [C II]/CO (3–2) line profiles in ALESS 49.1 and ALESS 57.1. The moment-1 maps reveal a clear velocity gradient across both ALESS 49.1 and ALESS 57.1. The spectra were extracted from the naturally weighted channel maps, using an aperture 1 arcsec (~8 kpc) in radius for CO (3–2) and 0.″5 (~4 kpc) in radius for [C II], given the compact size of the [C II] emission.

The [C II] line profile in ALESS 49.1 largely traces the CO (3–2) profile, exhibiting an increased brightness in the blue channels. In ALESS 49.1, we find a tentative (2.5σ–3σ) increase in the [C II]/CO (3–2) ratio between the center ($\pm$200 km s^{-1}) and the wings ($\pm$(200–600) km s^{-1}) of the lines. This might be due to (1) a significant fraction of the [C II] emission in the reddest and bluest channels being very extended and thus resolved out by our Band 8 imaging or (2) a spatial variation in the gas conditions. The [C II]/CO (3–2) ratio in ALESS 57.1 is consistent with being constant across the full velocity range.

We model the velocity fields using the GALPAK3D software (Bouché et al. 2015). GALPAK3D uses a Monte Carlo approach to extract the kinematic and morphological parameters from three-dimensional image cubes, accounting for both the spatial and spectral response of the instrument, assuming a parametric model for a rotating disk. For our simulations, we assume an exponential disk profile—an appropriate choice for ALESS SMGs, which show a mean Sérsic index of $n = 0.9 \pm 0.2$ (Hodge et al. 2016; $n = 1$ corresponds to an exponential profile). To improve the S/N and the speed of the calculations, we resampled our data onto cubes with a pixel size of 25 mas, using natural weighting.

Figure 5 shows the input and reconstructed moment-0 and moment-1 maps for ALESS 49.1 and ALESS 57.1. At the S/N of our Band 8 observations, velocity fields in both sources are consistent with an ordered, disk-like rotation. The deconvolved [C II] rotational curves are shown in Figure 6, which also lists the FWHM velocity measurements obtained from the fitting of the spatially integrated CO (3–2) spectra (Calistro Rivera et al. 2018). The source inclinations are inferred by fitting the

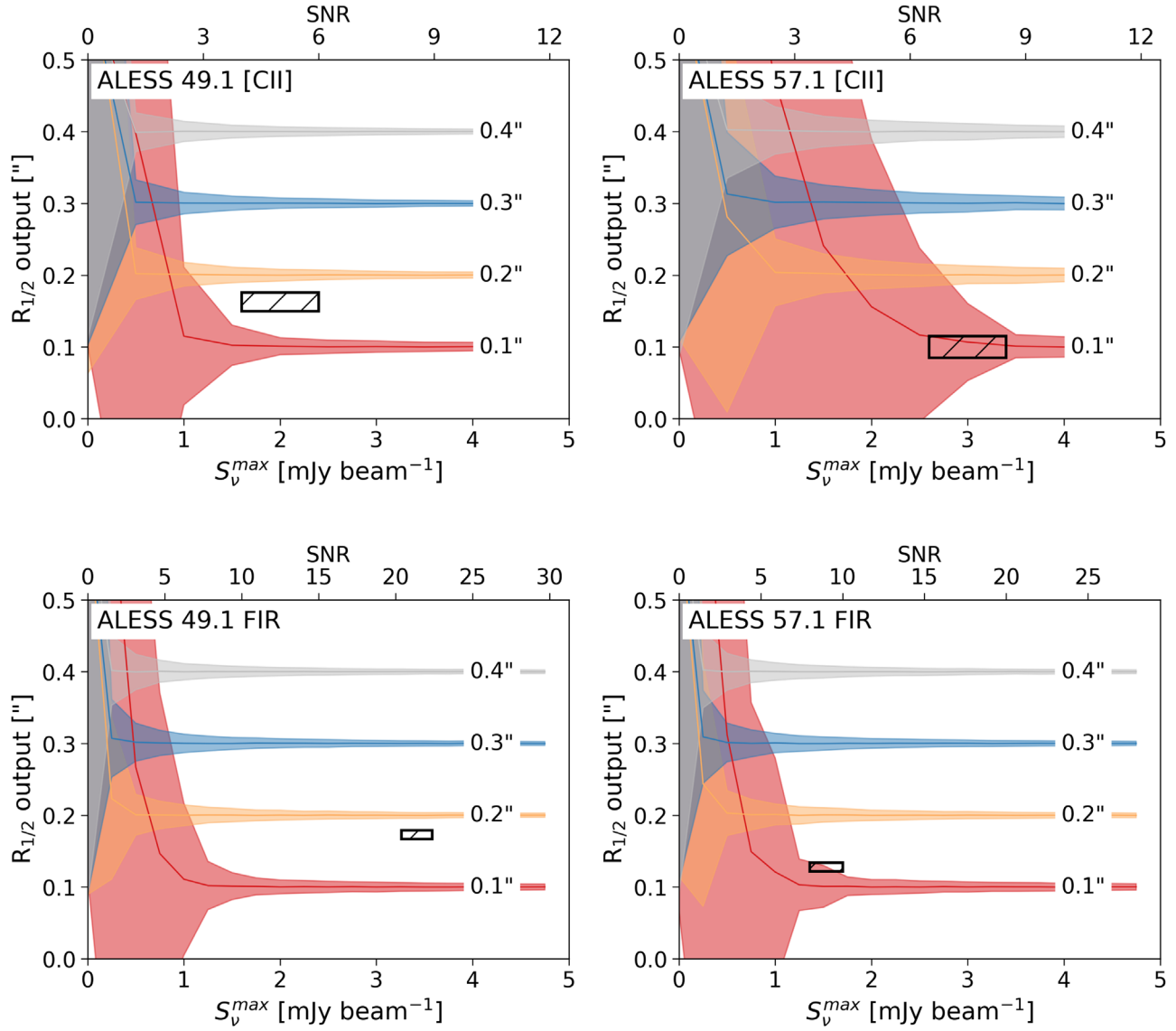

Figure 3. Comparison of the inferred and true $R_{1/2}$ for the [C II] line (top) and 160 μm data continuum (bottom). The thick lines denote the mean inferred $R_{1/2}$ for input $R_{1/2} = 0.1$–$0\farcs4$, with colored regions denoting the 1σ uncertainty from the u-v plane fitting only. For $R_{1/2} > 0\farcs4$, the source sizes are inferred robustly and are not shown for clarity. The boxed regions indicate the measured source sizes and peak surface brightness for ALESS 49.1 and ALESS 57.1 with 1σ uncertainties. Given the S/N of our observations, we rule out the possibility that [C II] and 160 μm continuum follow the same single-Gaussian profile as the CO (3–2) emission.

moment-0 map and agree with those derived from CO (3–2) imaging by Calistro Rivera et al. (2018) within 1σ–2σ uncertainty.

3.4. SED Modeling

We infer the global stellar and ISM properties of ALESS 49.1 and ALESS 57.1 from the spatially integrated SEDs using the MAGPHYS package (da Cunha et al. 2008), specifically its high-redshift extension (da Cunha et al. 2015). These differ from the previously published SEDs (da Cunha et al. 2015) by using the CO (3–2)-derived spectroscopic redshifts, compared to the photometric ones from da Cunha et al. (2015), and inclusion of ALMA Band 3/4/8 continuum flux densities. Namely, in addition to the Band 8 continuum measurements from Table 1, we include Band 4 continuum measurements ($S_{2.1\ \mathrm{mm}} = 380 \pm 100\ \mu$Jy and $65 \pm 50\ \mu$Jy for ALESS 49.1 and ALESS 57.1, respectively; E. da Cunha et al. 2019, in preparation), as well as the ALMA Band 3 continuum measurement for ALESS 49.1 ($S_{3.3\ \mathrm{mm}} = 37 \pm 5\ \mu$Jy; Wardlow et al. 2018).

The MAGPHYS-inferred source properties are listed in Table 2; the observed multiwavelength photometry and MAGPHYS SED models are provided in Appendix B. The estimated dust temperatures $T_{\mathrm{dust}} = 46^{+6}_{-2}$ K and 51^{+7}_{-1} K in ALESS 49.1 and ALESS 57.1, respectively, are warmer than the median $T_{\mathrm{dust}} = 42 \pm 2$ K of the ALESS SMGs inferred from MAGPHYS modeling (da Cunha et al. 2015). The more precise spectroscopic redshifts and additional ALMA photometry result in a temperature increase compared to values reported by da Cunha et al. (2015), $T_{\mathrm{dust}} = 46^{+0}_{-3}$ K and 43^{+15}_{-14} K, respectively. Elevated T_{dust} in intensely star-forming $z \sim 4.5$ galaxies was reported by Cooke et al. (2018), who interpret the inferred median $T_{\mathrm{dust}} = 55 \pm 4$ K as evidence for high Σ_{SFR} at high redshift. Note that the da Cunha et al. (2015) and Cooke et al. (2018) models use *Herschel* SPIRE and ALMA Band 7 photometry, while our models include ALMA

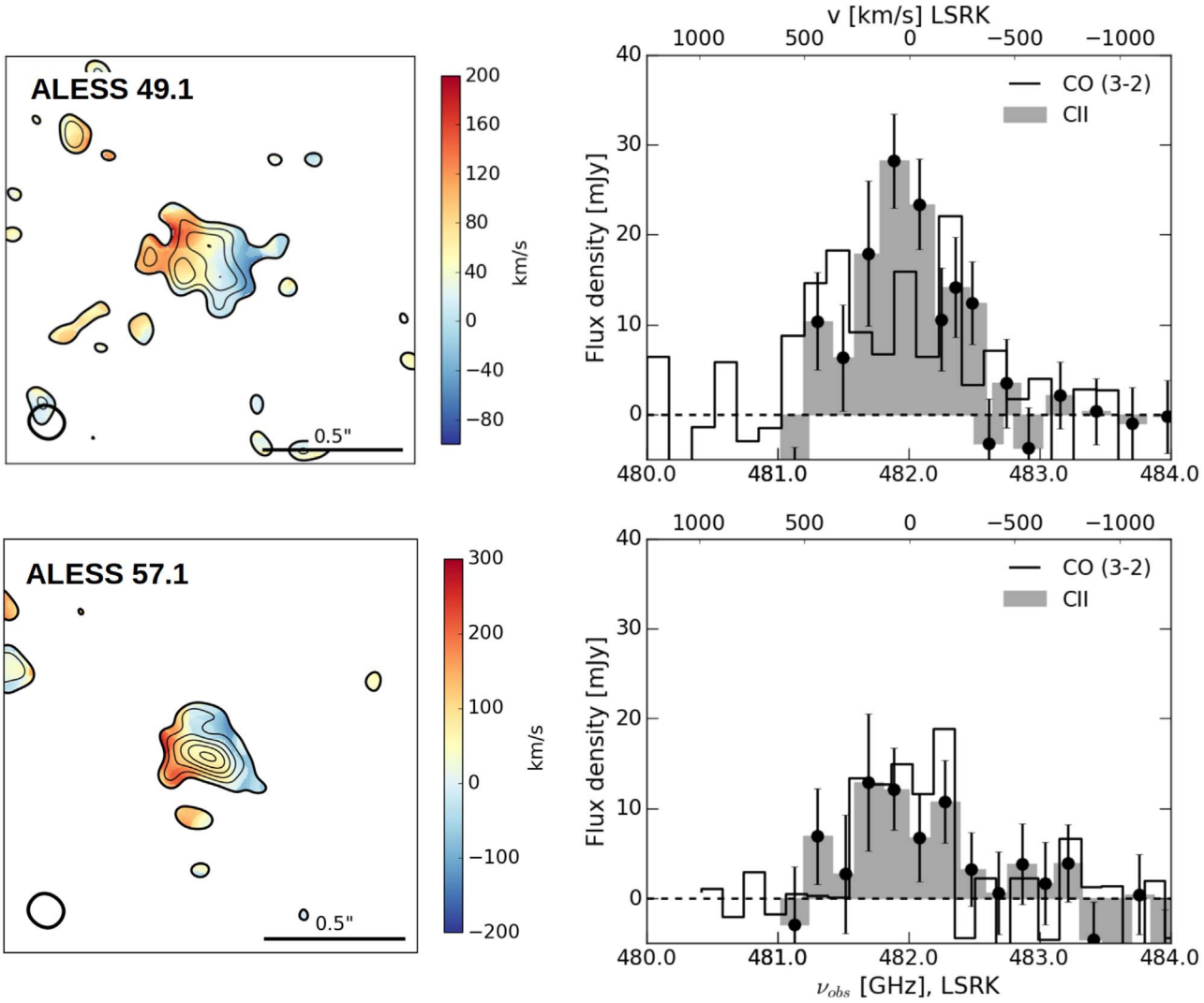

Figure 4. Moment-1 (velocity) maps and [C II] line profiles for ALESS 49.1 and ALESS 57.1. The contours correspond to [C II] moment-0 maps as shown in Figure 1. The [C II] velocity fields in both galaxies show a clear gradient across the source, without any major perturbations. The CO (3–2) spectra are taken from Calistro Rivera et al. (2018); the CO (3–2) flux density is scaled up by a factor of 10 for clarity. The velocity is given in the LSRK frame with respect to the redshift of $z = 2.943$, using the radio definition of velocity. The line intensity was measured from images obtained using natural weighting, for an aperture with 1 arcsec and $0\farcs5$ diameter for CO (3–2) and [C II] emission, respectively, centered on the surface brightness maximum of the 160 μm continuum. The error bars indicate 1σ uncertainty. The frequency coverage of our Band 8 observations does not extend below 481.0 GHz. The [C II] and CO (3–2) line widths match each other (Table 1).

Band 3, 4, and 8 observations, thus better sampling the Rayleigh–Jeans tail of dust thermal spectrum. Compared to the MAGPHYS models of the entire ALESS sample (da Cunha et al. 2015), ALESS 49.1 and ALESS 57.1 have SFRs higher by a factor of $\sim$2 (da Cunha et al. 2015: median SFR $= 280 \pm 70$ $M_\odot\,\mathrm{yr}^{-1}$) and stellar masses a factor of 2 lower (da Cunha et al. 2015: $M_* = (8.9 \pm 0.1) \times 10^{10}$ $M_\odot\,\mathrm{yr}^{-1}$); the dust mass is consistent with the median da Cunha et al. (2015) value ($(5.6 \pm 1.0) \times 10^{10}\,M_\odot$). The gas depletion timescale $M_{\mathrm{gas}}/\mathrm{SFR}$ is 100 ± 40 Myr in both ALESS 49.1 and ALESS 57.1, in line with $z \simeq 2$–4 SMGs (Bothwell et al. 2013; Huynh et al. 2017), and a few times lower than claimed for $z = 1$–3 massive main-sequence galaxies from the PHIBBS survey (0.7 ± 0.1 Gyr; Tacconi et al. 2018).

Using the SED models, we can estimate the fraction of the 160 μm continuum that is resolved out by comparing the observed rest-frame 160 μm continuum fluxes with SED modeling predictions, assuming constant T_{dust} and optical depth across the source. Namely, we use MAGPHYS to perform SED modeling using all the photometry points apart from the rest-frame 160 μm continuum. The predicted 160 μm flux densities are 11.8 and 7.6 mJy for ALESS 49.1 and ALESS 57.1, respectively; the observed flux densities match the predicted ones within $<$10%. Therefore, we conclude that our observations recover the bulk of the 160 μm emission, in line with the compact continuum sizes inferred in Section 3.2.

4. Discussion

4.1. Comparison with CO (3–2) Emission

Based on the *u-v* plane analysis in Section 3.2, which was tested on mock ALMA data in Section 3.2.1, we found the [C II]/160 μm continuum surface brightness distribution to be dominated by a compact component, embedded within a low surface brightness, extended emission. We now compare these morphologies to the CO (3–2) surface brightness profiles and other low- and high-redshift observations and simulations.

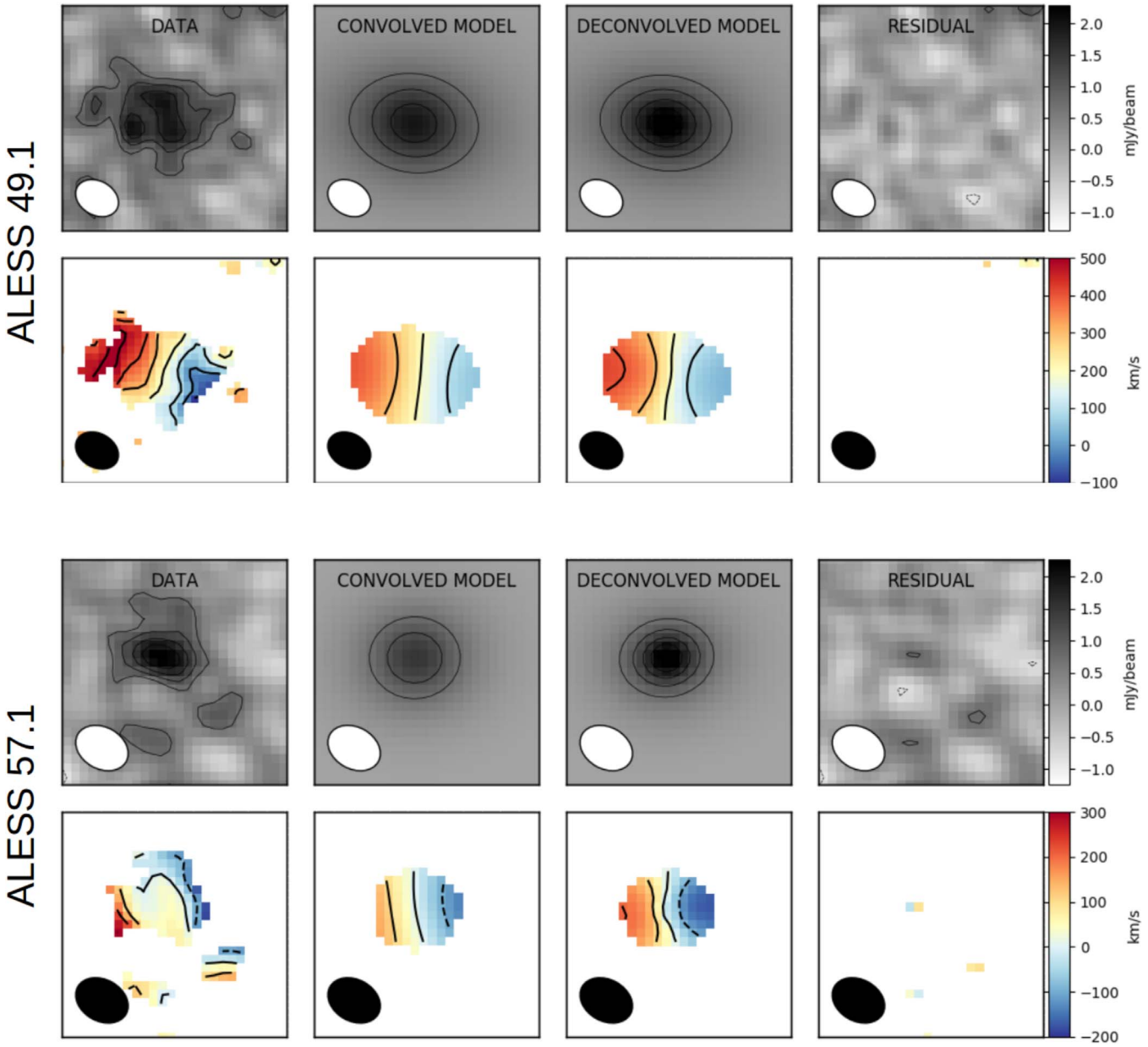

Figure 5. GALPAK3D models of the [C II] velocity field in ALESS 49.1 (top) and ALESS 57.1 (bottom), using an exponential disk model. The top row shows, from left to right, the velocity moment-0 (surface brightness) data, the best moment-0 model convolved with the beam, the best moment-0 model (deconvolved), and the moment-0 residuals. The moment-0 contours start at $\pm 2\sigma_{\rm rms}$ level and increase in steps of $1\sigma_{\rm rms}$. The moment-1 contours are drawn in steps of ± 100 km s^{-1}. The bottom row shows the reconstructed moment-1 (velocity) maps for regions with surface brightness $>2\sigma_{\rm rms}$. The velocity maps are consistent with the exponential disk model, with no residuals at $>2\sigma_{\rm rms}$ significance. The FOV size is $1.6 \times 1\farcs6$ and $1.4 \times 1\farcs4$, respectively.

4.1.1. 160 μm Continuum Size

Comparing the 160 μm continuum emission sizes with the CO (3–2) sizes (Table 2), the 160 μm continuum is 1.9 ± 0.3 (ALESS 49.1) and 3.1 ± 0.7 (ALESS 57.1) more compact than the CO (3–2) emission.

Compact dust continuum emission embedded in a larger molecular gas reservoir has been observed in a number of high-resolution studies of $z = 2$–4 SMGs. For example, Plateau de Bure Interferometer (PdBI)/Very Large Array (VLA) imaging of GN20 ($z = 4.05$) revealed a compact dusty, star-forming region within a large disk as traced by the CO (2–1) emission (Hodge et al. 2012, 2015). At very high spatial resolutions ($\sim$100 pc), similar morphology has been seen in the strongly lensed $z = 3$ SMG SDP.81 (ALMA Partnership et al. 2015), which shows a compact ($\sim$3 kpc across), dusty star-forming disk (Rybak et al. 2015a), embedded in a large ($\geqslant$10 kpc) molecular gas reservoir, as traced by the CO (1–0) emission (Valtchanov et al. 2011; Rybak et al. 2015b). Similarly, Spilker et al. (2015) observed compact ALMA Band 7 continuum and extended CO (3–2)/CO (1–0) emission in two strongly lensed galaxies from the South Pole Telescope sample; note that in SMGs the CO (3–2) is typically significantly less extended than the CO (1–0) line (e.g., Ivison et al. 2011; Riechers et al. 2011). Using ALMA 860 μm continuum, ALMA CO (3–2), and SINFONI Hα observations of ALESS 67.1 ($z = 2.1$), Chen et al. (2017) found the ALMA continuum to be a factor of $\sim$5 more compact than CO (3–2) and Hα emission (which are similar in size). Finally, Calistro Rivera et al. (2018) compared

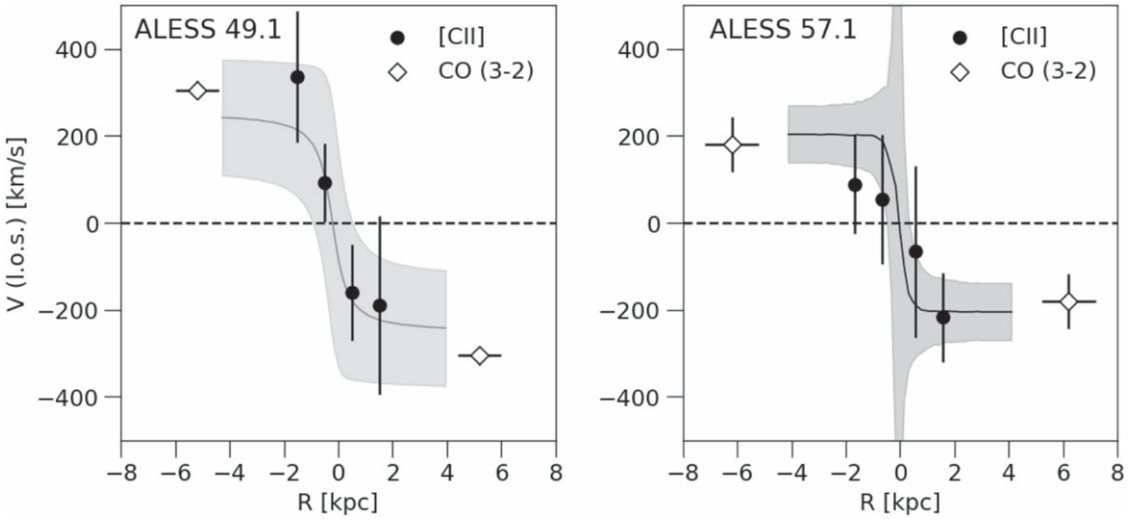

Figure 6. Line-of-sight velocity curves for ALESS 49.1 and ALESS 57.1, showing the [C II] velocity and velocity dispersion measured from the image cubes (filled circles), with rotation curves inferred from GALPAK3D (solid line; velocity dispersion estimate indicated by the shaded region), alongside the CO (3–2) measurements (open diamonds; Calistro Rivera et al. 2018). The [C II] measurements were extracted along the major kinematic axis determined by the GALPAK3D modeling from an aperture one beamwidth wide. The line-of-sight velocity flattens out at ∼2 kpc radius, suggesting disk-dominated kinematics. The large GALPAK3D-predicted velocity dispersion at the center of ALESS 57.1 is a numerical artifact.

stacked ALMA observations of CO (3–2) and 860 μm continuum (Hodge et al. 2016) of a sample of 4/18 SMGs from the ALESS sample, showing the FIR continuum to be more compact by a factor of >2. Based on a radiative transfer modeling, Calistro Rivera et al. (2018) found that the compact FIR and extended CO (3–2) sizes are consistent with a decrease in dust temperature and optical depth toward the outskirts of the source. The compact continuum sizes in ALESS 49.1 and ALESS 57.1 thus add to the growing evidence for variations in ISM conditions in SMGs on scales of a few kiloparsecs.

4.1.2. [C II] Emission Size

Based on the source sizes inferred from *u-v* plane fitting, the [C II] emission is 2.0 ± 0.4 (ALESS 49.1) and 3.9 ± 0.7 (ALESS 57.1) times more compact than CO (3–2). The compact size of the high surface brightness [C II] component contrasts with a relatively similar extent of the [C II] and low-*J* CO emission in local galaxies, as presented by de Blok et al. (2016), who found the [C II] to be "*slightly less compact than the CO*" (scale radius ∼70% ± 20% larger). Note that the de Blok et al. (2016) galaxies have $\Sigma_{\rm SFR} \simeq 10^{-3}$ to 10^{-2} $M_\odot\,{\rm yr}^{-1}\,{\rm kpc}^{-2}$, >3 dex lower than ALESS 49.1 and ALESS 57.1.

The [C II] morphologies, consisting of a high surface brightness compact and a low surface brightness, extended component, have been observed in several local star-forming galaxies. For example, Kuiper Airborne Observatory imaging of the [C II] emission in NGC 6946 (Madden et al. 1993) resolved three distinct components: (1) a bright, compact nucleus ($R < 300$ pc); (2) a faint, diffuse component at least 12 kpc in radius, contributing ∼40% of the total [C II] flux (Contursi et al. 2002); and (3) local enhancements corresponding to the spiral arms.

Similarly, one of the best-studied $z \geqslant 5$ sources with resolved [C II]/low-*J* CO observations—$z \sim 6.42$ quasar SDSS J1148+5251 (Walter et al. 2004, 2009)—has a compact ($R \sim 0.75$ kpc) [C II] emission embedded within a much more extended ($R \sim 2.5$ kpc) CO (3–2) reservoir (Walter et al. 2009; Stefan et al. 2015). Using sensitive PdBI observations, Cicone et al. (2015) found an extremely extended (out to ∼30 kpc) [C II] emission associated with powerful outflows likely driven by the central engine in J1148+5251.

Apart from observational evidence, a compact, high surface brightness [C II] component in star-forming galaxies has been predicted by simulations. In particular, using zoom-in cosmological SPH simulations of several mildly star-forming $z \sim 2$ galaxies (SFR = 5–60 $M_\odot\,{\rm yr}^{-1}$), Olsen et al. (2015) predicted that the [C II] emission is concentrated into a compact central region ($R \sim 1$ kpc), with a much fainter (by up to 1 dex) extended component—similar to our double-component model of [C II] emission in ALESS 49.1. In the Olsen et al. (2015) simulations, the compact size of the [C II] emission is due to gas inflows into the central star-forming regions, and the [C II] emission is dominated by the dense, molecular phase of the ISM. This contrasts with low-SFR galaxies, where the bulk of the star formation takes place in the spiral arms at large galactocentric radii (e.g., *Herschel* survey of the Milky Way [C II] emission; Pineda et al. 2013).

4.1.3. Inferring FIR Source Sizes Using the Stacey et al. (2010) Relation

Given the limited angular resolution of many high-redshift [C II] detections, the source size cannot be inferred directly from unresolved/marginally resolved data. However, parallel [C II]/CO/FIR continuum observations have been used to constrain the source size, assuming that the bulk of the line and continuum emission originates in PDRs.

This technique, introduced by Stacey et al. (2010), compares the observed [C II]/CO/FIR fluxes with predictions from the PDR models of Kaufman et al. (1999, see Section 4.4) to infer the far-UV (FUV) field strength G_0 and the density n. The observed $L_{\rm FIR}$ and inferred G_0 are then used to infer the FIR size $R_{\rm FIR}$ using the Wolfire et al. (1990) relations. In particular, Wolfire et al. (1990) distinguish two main regimes:

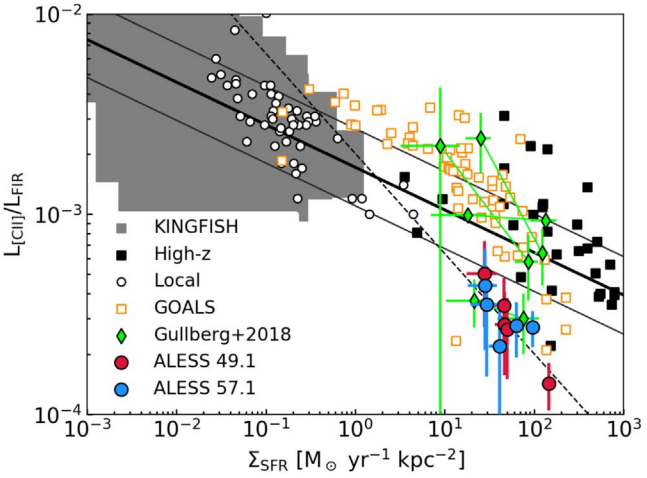

Figure 7. Resolved [C II]/FIR deficit in ALESS 49.1 and ALESS 57.1, compared to the KINGFISH (Smith et al. 2017) and GOALS (Díaz-Santos et al. 2017) samples and other local (open circles) and high-redshift measurements (black filled squares), adapted from Smith et al. (2017) and Gullberg et al. (2018). For each of the Gullberg et al. (2018) sources, we show the ratio for the inner and outer region, connected by a line. The thick black lines indicate the Smith et al. (2017) empirical fit to the [C II]/FIR data (Equation (3) and the corresponding 1σ scatter; the dashed line indicates the prediction from the Muñoz & Oh 2016 temperature-saturation model (Equation (5)), for $f_{[C\,II]} = 0.13$. The resolved ALESS 49.1 and ALESS 57.1 data points fall below the Smith et al. (2017) trend and follow a much steeper slope, indicating a [C II]-saturation regime. The error bars on ALESS 49.1 and ALESS 57.1 measurements include a contribution from extended [C II]/160 μm continuum components.

1. $\langle\lambda_{FUV}\rangle < R_{FIR}$

$$\langle G_0\rangle = 3 \times 10^4 \left(\frac{L_{FIR}}{10^{10} L_\odot}\right)\left(\frac{\langle\lambda_{FUV}\rangle}{100\ \mathrm{pc}}\right)\left(\frac{100\ \mathrm{pc}}{R_{FIR}}\right)^3 \times (1 - \exp(-R_{FIR}/\langle\lambda_{FUV}\rangle)), \quad (1)$$

2. $\langle\lambda_{FUV}\rangle \geqslant R_{FIR}$

$$\langle G_0\rangle = 3 \times 10^4 \left(\frac{L_{FIR}}{10^{10} L_\odot}\right)\left(\frac{100\ \mathrm{pc}}{R_{FIR}}\right)^2, \quad (2)$$

where G_0 is given in the units of the Habing field (1.6×10^{-3} erg cm^{-2} s^{-1}) and R_{FIR} and the FUV photon mean free path $\langle\lambda_{FUV}\rangle$ are in parsecs. Stacey et al. (2010) assume that $\langle\lambda_{FUV}\rangle$ in $z = 1$–2 star-forming galaxies is the same as in the nearby starburst M82. For M82, Stacey et al. (2010) assume $L_{FIR} = 2.8 \times 10^{10}\ L_\odot$, $G_0 = 10^3$, and $R_{FIR} = 150$ pc.

With high-resolution [C II], CO (3–2), and FIR observations and robust source sizes in hand, we now investigate the applicability of the Stacey et al. (2010) relations to high-redshift SMGs. Assuming that $\langle\lambda_{FUV}\rangle$ is smaller than R_{FIR} (an appropriate choice given the heavily obscured, dusty environment), we infer $R_{FIR} = 410 \pm 50$ pc and 420 ± 70 pc for ALESS 49.1 and ALESS 57.1, respectively, a factor of 2.5–3.5 smaller than the actual FIR half-light radii measured from the *u-v* plane fitting (Section 3.2). We note that the L_{FIR}, G_0, and R_{FIR} estimates for M82 from the literature show a considerable scatter; alternatively, the $\langle\lambda_{FUV}\rangle$ in SMGs might be somewhat longer than that in the central region of M82. Crucially, if the FIR sizes of high-redshift SMGs are systematically underestimated by similar factors, the SFR surface density $\Sigma_{SFR} \propto L_{FIR}/R_{FIR}^2$ will be *overestimated* by 0.5–1.0 dex—a shift that might affect a number of unresolved observations in, e.g., the [C II]/FIR—Σ_{SFR} plane (Figure 7).

4.2. Molecular Gas Kinematics

The [C II] and CO (3–2) lines provide two independent measurements of the molecular gas velocity structure. Due to their different spatial extents (Section 3.2), the [C II] and CO (3–2) emissions trace the velocity field at different radii. Figure 6 shows the line-of-sight velocity as traced by the [C II] and CO (3–2) emissions and the GALPAK3D model of the [C II] disk. In particular, the [C II] emission probes the velocity field within the inner 2 kpc region. Typically, rotational curves of disk-like galaxies are decomposed into contributions from the dark matter halo, and baryons in the form of a galactic bulge and disk. Given that the baryonic mass $M_{bar} = M_* + M_{gas}$ (Table 2) is comparable to the dynamical mass enclosed within twice the CO (3–2) half-light radius (5.2 and 6.0 kpc in ALESS 49.1 and ALESS 57.1, respectively; Table 2), we conclude that the inner rotation curves are baryon dominated.

In both ALESS 49.1 and ALESS 57.1, the line-of-sight velocity v_{los} flattens at 2–4 kpc radius. As a dominant bulge would cause the v_{los} to flatten rapidly on scales of a few hundred parsecs (e.g., Sofue et al. 1999), whereas the v_{los} profiles in ALESS 49.1 and ALESS 57.1 are still rising at $R \geqslant 1$ kpc, we speculate that the inner ($R \leqslant 2$ kpc) rotational curves in ALESS 49.1 and ALESS 57.1 do not yet have a significant bulge component and hence are disk dominated. However, higher-S/N data are necessary to confirm this hypothesis.

The rotation curves have been studied at a comparable resolution in only a handful of SMGs. In this respect, ALESS 49.1 and ALESS 57.1 velocity fields are most directly comparable to those in $z = 2.4$ twin hyperluminous SMGs H-ATLAS J084933 (Ivison et al. 2013) and strongly lensed SMGs SMM J2135-0102 ($z = 2.03$; Swinbank et al. 2011) and SDP.81 ($z = 3.04$; Dye et al. 2015; Rybak et al. 2015b), which flatten out at $\sim$200 km s^{-1} within the inner 2 kpc radius. The dynamical mass enclosed within the central 2 kpc radius region of ALESS 49.1 and ALESS 57.1 is M_{dyn} ($R \leqslant 2$ kpc) = $(6.2 \pm 5.5) \times 10^{10}\ M_\odot$ and $(2.7 \pm 1.6) \times 10^{10}\ M_\odot$, respectively; although CO (3–2) observations provide mass estimates at 5–6 kpc radius, the large uncertainties prevent us from investigating the mass profiles of the two sources. The limited extent of the bright [C II] component and the possibility that an extended [C II] emission in ALESS 49.1 is resolved out highlight the difficulties of using very high angular resolution observations to trace the kinematics of the cold gas reservoir.

4.3. The Resolved [C II]–FIR Ratio

The high resolution of ALMA Band 8 data allows us to investigate the $L_{[C\,II]}/L_{FIR}$ ratio at $z \sim 3$ on 1 kpc scales. Here we focus on the *central region* ($R \leqslant 2$ kpc), in which the contribution of any extended [C II] component is below 20%. This discussion does not include the *global* tracer ratios, as the Band 8 observations might resolve out a significant fraction of the total [C II] flux from an extended component.

The SFR surface density Σ_{SFR} is estimated by adopting the global SFR from our SED fits in Section 3.4, assuming (1) a linear mapping between the rest-frame 160 μm emission and SFR, (2) no AGN contribution to the rest-frame FIR luminosity, and (3) a universal initial mass function (c.f.

Zhang et al. 2018b). The linear mapping between the FIR continuum and SFR density assumes a constant dust temperature and opacity across the source. Further high-resolution, multiband observations of the dust continuum and spatially resolved SED modeling would be required for a more precise $\Sigma_{\rm SFR}$ estimate for different parts of the source. The [C II]/FIR ratio was extracted by binning the [C II] and 160 μm continuum maps (Figure 1) into pixels 1 beamwidth large; only pixels for which both the [C II] and 160 μm continuum have S/N $\geqslant 2$ are considered.

Figure 7 shows the resolved $L_{\rm [C\,II]}/L_{\rm FIR}$ for ALESS 49.1 and ALESS 57.1 as a function of the SFR surface density $\Sigma_{\rm SFR}$, compared to resolved and unresolved measurements from both local and high-redshift sources (Díaz-Santos et al. 2017; Smith et al. 2017; Gullberg et al. 2018 and references therein). In both ALESS 49.1 and ALESS 57.1, the resolved ratio decreases sharply with $\Sigma_{\rm SFR}$, confirming the [C II]/FIR deficit on 1 kpc scales.

Comparing our measurements with an empirical relation between [C II]/FIR ratio and $\Sigma_{\rm SFR}$ proposed by Smith et al. (2017),

$$\Sigma_{\rm SFR} = (12.7 \pm 3.2)\left(\frac{L_{\rm [C\,II]}/L_{\rm FIR}}{0.001}\right)^{-4.7\pm0.8} M_\odot\ {\rm yr}^{-1}\ {\rm kpc}^{-2}. \quad (3)$$

We find that the bulk of the ALESS 49.1 and ALESS 57.1 [C II]/FIR measurements are below the 1σ scatter of the Smith et al. (2017) relation, with $\Sigma_{\rm SFR}$ almost 1–2 dex lower than those predicted by the Smith et al. (2017) relation. This suggests that the Smith et al. (2017) $\Sigma_{\rm SFR}$—$L_{\rm [C\,II]}/L_{\rm [C\,II]}$ might not be directly applicable in the high-$\Sigma_{\rm SFR}$ regime in ALESS 49.1 and ALESS 57.1.

We note that the ALESS 49.1 and ALESS 57.1 [C II]/FIR measurements fall below the redshift $z \sim 4.5$ resolved measurements of Gullberg et al. (2018). This can be attributed to several factors: (1) different source selection; (2) aperture-averaging effects in Gullberg et al. (2018), as the [C II]/FIR ratio is calculated for apertures several kiloparsecs wide; and (3) systematic uncertainties such as Gullberg et al. (2018) assuming $T_{\rm dust} = 50 \pm 4$ K for all their sources. Regarding source selection, ALESS 49.1 and ALESS 57.1 have $L_{\rm FIR}$ more than 2$\times$ higher than Gullberg et al. (2018) sources, while being more compact in the rest-frame FIR continuum; consequently, our measurements might probe a higher-$\Sigma_{\rm FIR}$ regime, which would correspond to lower [C II]/FIR ratio and potentially higher $T_{\rm gas}$ (see Section 4.4).

The radial variation of $L_{\rm [C\,II]}/L_{\rm FIR}$ in ALESS 49.1 and ALESS 57.1 is shown in Figure 8. Fitting the resolved [C II]/FIR data with a power law $L_{\rm [C\,II]}/L_{\rm [C\,II]} \propto R^{\alpha}$, we find strong evidence for a radial variation of the [C II]/FIR ratio in ALESS 49.1 ($\alpha = 0.41 \pm 0.06$), while in ALESS 57.1 the slope is consistent with being flat ($\alpha = 0.05 \pm 0.05$). A decrease in the [C II]/FIR ratio toward the center of the source is seen in both local star-forming galaxies (e.g., Madden et al. 1993; Smith et al. 2017) and high-redshift sources (Gullberg et al. 2018) and indicates that the [C II]/FIR deficit is driven by local processes, as opposed to global properties of the sources. In particular, Smith et al. (2017) found the [C II]/FIR ratio to be suppressed by on average 30% ± 15% in the central $R \leqslant 400$ pc regions of galaxies without an AGN. On the other hand, the [C II]/FIR ratio drops by a factor of a few over the inner 2 kpc in nuclear starbursts in M82 and M83 (Herrera-Camus et al. 2018). While the *Chandra*-detected obscured AGN in ALESS 57.1 (Wang et al. 2013) might be expected to suppress the [C II] emission in the circumnuclear region, we do not detect any strong [C II] suppression in ALESS 57.1 on 1 kpc scales. The difference in the [C II]/FIR radial profiles in ALESS 49.1 and ALESS 57.1 is driven by the larger scatter in [C II]/FIR ratio for a given $\Sigma_{\rm SFR}$ in ALESS 57.1 (see Figure 7), which is a result of the complex [C II] and 160 μm morphology in that source (Figure 1). Note that the limited S/N of our data at $R \geqslant 2$ kpc prevents us from studying the [C II]/FIR radial dependence at larger radii.

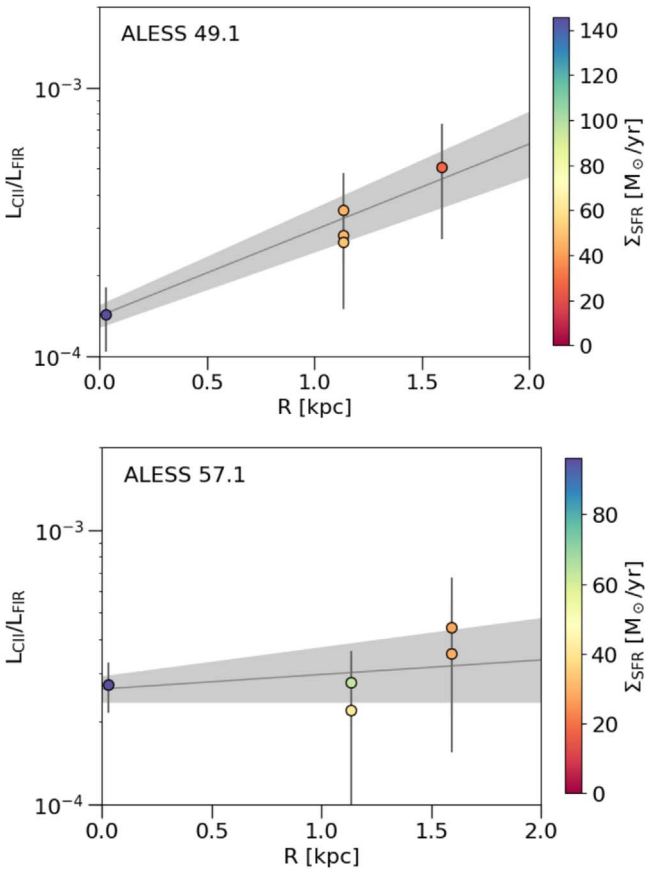

Figure 8. [C II]/FIR deficit radial trends in ALESS 49.1 and ALESS 57.1, color-coded by the SFR surface density $\Sigma_{\rm SFR}$; each point corresponds to a separate resolution element. The lines and shaded regions indicate the best-fitting slopes and corresponding uncertainties, respectively. The radial distances R are measured from the 160 μm continuum surface brightness maximum. The data used to create this figure are available.

4.4. Comparison with PDR Models

The relative intensities of the [C II], CO (3–2), and FIR emission from hot dissociation regions (PDRs) depend on the ionizing FUV field strength G_0 and the gas density n(H), which determine the depth of the outer C^+ layer. We now use our resolved [C II]/CO (3–2)/FIR observations to infer the G_0 and n using the PDR models from the PDRTOOLBOX library (Kaufman et al. 2006; Pound & Wolfire 2008). We focus on the central regions of the source ($R \leqslant 2$ kpc), adopting the best-fitting models from Section 3.2.

For a proper comparison, several corrections need to be applied. First, the [C II] emission from the ionized ISM needs to be subtracted from the observed [C II] signal. The contribution from the ionized gas can be estimated from [N II] 122 μm/205 μm lines, which have similar critical density for collisions with electrons (300 cm^{-3}/32 cm^{-3}) to the [C II] line (50 cm^{-3}; Goldsmith et al. 2012) but ionization energy >13.6 eV and hence trace only the ionized gas. Croxall et al. (2017) carried out a systematic study of the [N II] 122 μm/205 μm lines in a sample of 21 nearby star-forming galaxies, estimating the fraction of [C II] in PDRs as $f^{\rm PDR}_{\rm [C\,II]} \geqslant 0.8$ for sources with $\Sigma_{\rm SFR} \geqslant 10^{-2}\ M_\odot\,\mathrm{yr}^{-1}\,\mathrm{kpc}^{-2}$. At high redshift, Zhang et al. (2018a) used [N II] 122 μm line observations in $z = 1$–3 SMGs to derive 10%–15% ionized gas contribution to [C II] luminosity, assuming Galactic diffuse gas N and C abundances. Consequently, we adopt a conservative (i.e., low) estimate of $f^{\rm PDR}_{\rm [C\,II]} = 0.8$.

Second, PDRTOOLBOX models are derived for a one-dimensional, semi-infinite slab, illuminated from the face side only. In the intensely star-forming SMGs, we expect the clouds to be illuminated from multiple sides, and the optical thickness of individual tracers needs to be considered. Namely, for optically thick emission, only the emission from the side of the cloud facing the observer is observed; for the optically thin emission, the distant side of the cloud adds to the observed fluxes, and the line intensities expected from PDR models need to be multiplied by a factor of 2 (Kaufman et al. 1999). The 160 μm continuum is generally assumed to be optically thin. Based on the models of Narayanan & Krumholz (2014), the CO (3–2) line is expected to be optically thick with a median optical depth $\geqslant$10 for $\Sigma_{\rm SFR} = 10^{-1}$ to $10^{3}\ M_\odot\,\mathrm{yr}^{-1}$. The [C II] emission is optically thin in most environments, although there is evidence for moderately optically thick [C II] (optical depth $\sim$ 1) in both Galactic PDRs (Graf et al. 2012; Sandell et al. 2015) and high-redshift sources (Gullberg et al. 2015). Therefore, for an optically thin [C II], the predicted [C II]/CO (3–2) ratio has to be increased 2×; for an optically thick [C II], the predicted [C II]/FIR ratio has to be reduced by 1/2. We consider both optically thin and optically thick [C II] scenarios; however, as the evidence for optically thick [C II] is limited, we adopt the values derived for the optically thin [C II] for the rest of this paper.

Figure 9 shows the contours in the G_0/n space for the central $R \leqslant 2$ kpc region of ALESS 49.1 and ALESS 57.1, with best-fitting values listed in Table 3. The combination of the three tracers provides orthogonal constraints on G_0 and n. In particular, G_0 is largely determined by the [C II]/FIR ratio, and n by [C II]/CO (3–2). Table 3 lists the inferred G_0 and n values for the optically thin and optically thick [C II] scenarios, along with the PDR surface temperature. For the optically thin [C II] case, the conditions in ALESS 49.1 and ALESS 57.1 are almost identical, with $G_0 \sim 10^4$ and $n \sim 10^4$–$10^5\,\mathrm{cm}^{-3}$, implying a PDR surface temperature $T_{\rm PDR}$ of $\sim$700 K. Increasing the fraction of [C II] emission from the PDRs from 0.8 to 1.0 causes the inferred G_0 and n values to decrease by $\leqslant$0.25 dex. For the optically thick [C II] case, the inferred G_0 and n decrease by up to 0.5 and 1.0 dex, respectively; $T_{\rm PDR}$ is reduced to 400–500 K.

The G_0, n values in the central region of ALESS 49.1 and ALESS 57.1 are comparable to $G_0 = 10^3$–$10^{4.5}$, $n = 10^2$–$10^4\,\mathrm{cm}^{-3}$ inferred from unresolved observations of larger SMG samples, such as the [C II]/CO study of Stacey et al. (2010), the [C I]/CO study of 14 $z \geqslant 2$ SMGs by Alaghband-Zadeh et al. (2013), and FIR spectroscopy of lensed SMGs (Wardlow et al. 2017; Zhang et al. 2018a). Using [C II] and low-J CO observations in a sample of strongly lensed SMGs, Gullberg et al. (2015) found a larger scatter of FUV strength ($G_0 = 10^2$–8×10^3) and density ($n = 10^2$–$10^5\,\mathrm{cm}^{-3}$), although the effect of differential magnification might be substantial. For nearby star-forming galaxies, a comparison of observed spatially integrated [C II], [O I] 63 μm, and FIR luminosities with the PDRTOOLBOX models was carried out by Malhotra et al. (2001)

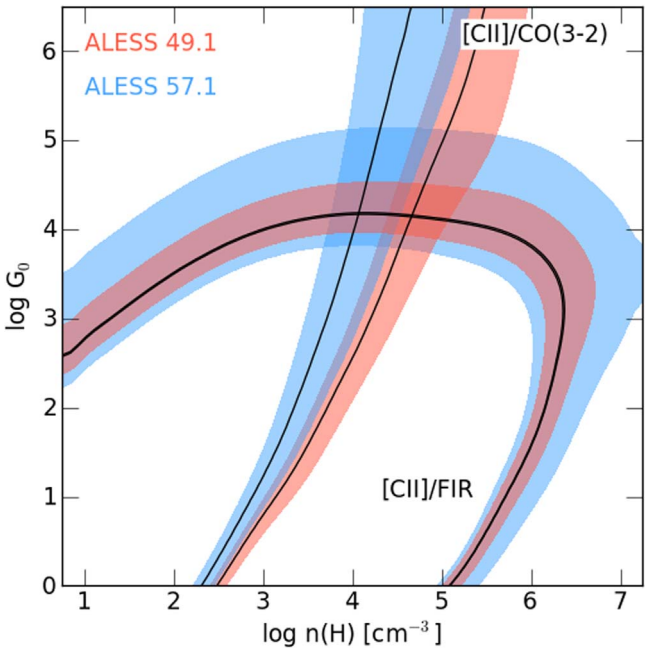

Figure 9. Constraints on the FUV field strength G_0 and density n for the central $R \leqslant 2$ kpc region derived from comparison with Kaufman et al. (2006) PDR models. For the [C II]/FIR/CO (3–2) emission, we adopt surface brightness profiles derived from the u-v plane fitting. The [C II] emission is assumed to be optically thin, with the PDR contributing 80% of the observed signal. The colored areas indicate 1σ confidence regions. For the central regions of ALESS 49.1 and ALESS 57.1, we infer $G_0 \sim 10^4$ and $n = 10^4$–$10^5\,\mathrm{cm}^{-3}$.

Table 3
Comparison with PDRTOOLBOX PDR Models: Observed [C II]/CO (3–2) and [C II]/FIR Continuum Ratios, along with Inferred FUV Field Strength G_0, Density n(H), and PDR Surface Temperature $T_{\rm PDR}$ for ALESS 49.1 and ALESS 57.1

Source		ALESS 49.1	ALESS 57.1
[C II]/FIR		$(3.3 \pm 1.5) \times 10^{-4}$	$(3.4 \pm 2.8) \times 10^{-4}$
[C II]/CO (3–2)		310 ± 100	600 ± 240
[C II] Optically Thin			
$\log G_0$		$4.1^{+0.3}_{-0.3}$	$4.2^{+0.9}_{-0.4}$
$\log n$(H)	(cm^{-3})	$4.7^{+0.4}_{-0.2}$	$4.1^{+0.5}_{-0.4}$
$T_{\rm gas}$	(K)	720 ± 200	670 ± 170
[C II] Optically Thick			
$\log G_0$		$3.8^{+0.3}_{-0.2}$	$3.7^{+1.0}_{-0.3}$
$\log n$(H)	(cm^{-3})	$3.9^{+0.4}_{-0.2}$	$3.4^{+0.4}_{-0.3}$
$T_{\rm gas}$	(K)	430 ± 30	480 ± 90

Note. We consider both optically thin and thick [C II] scenarios. The [C II] luminosities are given before subtracting the contribution from non-PDR sources.

and Díaz-Santos et al. (2017). ALESS 49.1 and ALESS 57.1 are consistent with the high-density Malhotra et al. (2001) sources; however, G_0 and n in ALESS 49.1 and ALESS 57.1 are higher than in the densest ultraluminous infrared galaxies (ULIRGs) from the Díaz-Santos et al. (2017) sample, which have $G_0 \sim 10^3$, $n = 1$–$10^3\,\mathrm{cm}^{-3}$. Note that the globally averaged G_0 and n in ALESS 49.1 and ALESS 57.1 might be lower than those inferred from the $R \leqslant 2$ kpc region. Finally, compared to the resolved kiloparsec-scale observations of local starburst galaxies NGC 6946 and NGC 1313 with inferred $G_0 = 10^3$–10^4, $n = 10^{3.0}$–$10^{3.5}\,\mathrm{cm}^{-3}$ (Contursi et al. 2002), the central regions of ALESS 49.1 and ALESS 57.1 show similar G_0 and somewhat higher n.

What drives the strong FUV fields in ALESS 49.1 and ALESS 57.1: a central AGN, or star formation? Although *Chandra* X-ray observations (Wang et al. 2013) revealed an obscured AGN in ALESS 57.1 (no emission from ALESS 49.1 was detected), it is unlikely that an obscured AGN would be driving a strong FUV field on few-kiloparsec scales. On the other hand, the G_0 in the vicinity of H II regions is of the order of 10^3–10^5 (e.g., Tielens & Hollenbach 1985; Hollenbach & Tielens 1999), comparable to the values inferred from our PDR models. Similarly, typical G_0 and n values for Galactic star-forming regions are of the order of $G_0 = 10^3$–10^5, $n = 10^3$–$10^6\,\mathrm{cm}^{-3}$ (Stacey et al. 1991, 2010). We therefore conclude that the strong FUV field in ALESS 49.1 and ALESS 57.1 is due to star formation, rather than a central AGN.

4.5. Origin of the [C II]/FIR Deficit

Having estimated G_0 and n in the central regions of ALESS 49.1 and ALESS 57.1, we now turn to the mechanism driving the [C II]/FIR deficit. We focus on the thermal saturation model proposed by Muñoz & Oh (2016) and the reduction of the photoelectric heating of the gas by small dust grains (e.g., Bakes & Tielens 1994; Malhotra et al. 2001); we briefly discuss other potentially relevant mechanisms—AGN contribution and dust-bounded H II regions—in Section 4.5.3. For a more exhaustive list of proposed mechanisms for the [C II]/FIR deficit, we refer the reader to Smith et al. (2017).

4.5.1. Thermal Saturation of the [C II] Line

Muñoz & Oh (2016) have proposed the thermal saturation of the upper level of the C^+ fine-structure transition as the main driver of the [C II]/FIR deficit. In other words, when $T_{\rm gas}$ exceeds the C^+ transition temperature (92 K), the upper-level/lower-level population ratio (and the [C II] luminosity) depends only weakly on $T_{\rm gas}$, while the FIR luminosity keeps on increasing.

Our PDRTOOLBOX models imply high FUV fields strength ($G_0 \sim 10^4$) and densities ($n = 10^4$–$10^5\,\mathrm{cm}^{-3}$) with gas surface temperatures larger than 500 K (Table 3). The [C II] transition is saturated in this regime. Following Muñoz & Oh (2016), the thermal cooling rate per hydrogen atom via the [C II] line depends on $T_{\rm gas}$ via

$$\Lambda_{\rm [CII]} = 2.3 \times 10^{-6}\, k_{\rm B}\, T_{\rm [CII]} \frac{2}{2 + \exp\left(T_{\rm CII}/T_{\rm gas}\right)} \frac{C}{H} \qquad (4)$$

where $k_{\rm B}$ is the Boltzmann constant, $T_{\rm [C\,II]}$ is the [C II] ionization temperature, and C/H are the relative abundances of the carbon and hydrogen atoms. Following Equation (4), the [C II] cooling rate increases by only ∼40% between $T_{\rm gas} = 100$ and 500 K, whereas the $L_{\rm FIR}$ increases by a factor of a few hundred, assuming that $T_{\rm dust}$ scales proportionally with $T_{\rm gas}$ and $L_{\rm FIR} \propto T_{\rm dust}^{4+\beta}$, where the dust opacity β is typically assumed to range from 1.5 to 2.5 (e.g., Casey et al. 2014).

For a more direct comparison with the Muñoz & Oh (2016) model, we compare the resolved [C II]/FIR observations in ALESS 49.1 and ALESS 57.1 (Figure 7) to the predicted $\Sigma_{\rm SFR}$-[C II]/FIR slope. According to Muñoz & Oh (2016), $L_{\rm [C\,II]}/L_{\rm FIR}$ ratio scales as

$$\frac{L_{\rm [C\,II]}}{L_{\rm FIR}} = 2.2 \times 10^{-3} \frac{f_{\rm C\,II}}{0.13} \left(\frac{\Sigma_{\rm FIR}}{10^{11} L_\odot\ \mathrm{kpc}^{-2}} \right)^{-1/2}, \qquad (5)$$

where $f_{\rm C\,II}$ is the fraction of gas emitting in [C II]. Fitting our data points with a power law following Equation (5), we obtain a best-fitting slope of $\gamma = -0.53 \pm 0.12$. This is in agreement with the thermal saturation model slope of $\gamma = -0.5$ (Equation (5)).

We note that Díaz-Santos et al. (2017) discount the thermal saturation of the [C II] line as a source of the [C II]/FIR deficit in local star-forming galaxies. Namely, comparing the [O I] 63 μm and [C II] line ratios with a statistical equilibrium radiative transfer model, they obtain a scaling between dust and gas kinetic temperature $T_{\rm gas} = (1.6$–$2.1) \times T_{\rm dust}$. Given $T_{\rm dust}$ of 21–48 K, they find $T_{\rm gas} \leqslant 92$ K, i.e., below the thermal saturation regime. However, ALESS 49.1 and ALESS 57.1 show relatively high global $T_{\rm dust} = 46^{+6}_{-2}$ and 51^{+7}_{-4} K, respectively (Table 2). Given the conversion factors from Díaz-Santos et al. (2017) and evidence for an increase in dust and gas temperature toward the center of SMGs (Calistro Rivera et al. 2018), we conclude that $T_{\rm gas}$ in the central regions of ALESS 49.1 and ALESS 57.1 likely exceeds 92 K.

4.5.2. Suppression of the [C II] Emission due to Positive Grain Charging

In addition to the thermal saturation, another potentially important effect of the G_0, n values inferred from our PDR analysis is the reduced photoelectric heating of the gas by electrons ejected from the small dust grains by the FUV photons (e.g., Bakes & Tielens 1994; Malhotra et al. 2001; Wolfire et al. 2003). At high G_0/n ratios, the grains become positively charged, thus raising the potential barrier for the electrons to escape.

Qualitatively, a reduced photoelectric heating will manifest in moderate $T_{\rm gas}/T_{\rm dust}$ ratios. Although ALESS 49.1 and ALESS 57.1 have elevated dust temperatures compared to other high-redshift SMGs (Swinbank et al. 2014; da Cunha et al. 2015) and local ULIRGs (Díaz-Santos et al. 2017), the high PDR surface temperatures indicate that the gas is already heated to high temperature, at which point the [C II] line becomes saturated.

Quantitatively, following Wolfire et al. (2003), the photoelectric heating rate per hydrogen atom is given as

$$\Gamma_{\rm PE} = \frac{1.1 \times 10^{-25} G' Z_d}{1 + 3.2 \times 10^{-2} [G' (T_{\rm gas}/100\ \mathrm{K})^{1/2} n_e^{-1} \phi_{\rm PAH}]^{0.73}} \times \mathrm{erg\ s^{-1}}, \qquad (6)$$

where $G' = 1.7 \times G_0$, Z_d is the dust-to-gas ratio (normalized to the Galactic value), n_e is the electron density, and $\phi_{\rm PAH}$ is a

factor associated with the polycyclic aromatic hydrocarbon molecules. The second term in the denominator corresponds to the positive grain charging. We follow Muñoz & Oh (2016) by adopting $n_e = 1.1 \times 10^{-4} n$, $\phi_{\rm PAH} = 0.5$. Note that Equation (6) assumes $T_{\rm gas} \leqslant 1000$ K, which is satisfied for both ALESS 49.1 and ALESS 57.1. While for the ALESS 49.1 and ALESS 57.1 values of G_0, n the second term in the denominator, corresponding to the reduction in photoelectric heating, becomes dominant, the numerator is also proportional to G_0. Comparing a typical nearby star-forming galaxy with $G_0 = 10^2$, $n = 10^4\,{\rm cm}^{-3}$ (see Muñoz & Oh 2016) and ALESS 49.1 and ALESS 57.1 with $G_0 = 10^4$, $n = 10^4\,{\rm cm}^{-3}$, the second term in the determinant increases from ∼0.3 to ∼18, indicating a significant reduction in the gas heating due to grain charging. However, at the same time, the overall $\Gamma_{\rm PE}$ *increases* by a factor of ∼6.

Therefore, we attribute the pronounced [C II]/FIR deficit in the central regions of ALESS 49.1 and ALESS 57.1 to the high gas temperature, which results in a quantum-level saturation of the C^+ fine structure.

4.5.3. Other Mechanisms for [C II]/FIR Deficit

Finally, we briefly consider other proposed mechanisms for the [C II] deficit.

AGNs can contribute to the [C II] deficit, both by increasing the FIR luminosity and reducing the C^+ abundance, and the [C II] emission by ionizing the carbon atoms to higher ionization states (C^{2+}, C^{3+}, etc.) via soft X-ray radiation (Langer & Pineda 2015). *Chandra* observations of ALESS 49.1 and ALESS 57.1 revealed an obscured AGN with an extinction-corrected X-ray luminosity of $\log L_{0.5-8.0\,{\rm keV}} = 44.3$ and no X-ray emission in ALESS 49.1 (Wang et al. 2013). According to Langer & Pineda (2015) models, for $n \sim 10^3\,{\rm cm}^{-3}$ (model closest to the conditions in ALESS 49.1 and ALESS 57.1), a 10% decrease in the fraction of carbon in the C^+ state requires an X-ray flux of $f_X \simeq 10^{3.5}$ erg cm^{-2} s^{-1}. Assuming that an X-ray flux dilutes with distance D as $1/4\pi D^2$, the AGN in ALESS 57.1 will affect only the innermost ∼100 pc radius, well below the spatial resolution of our data. Consequently, we do not expect a significant AGN contribution to the observed [C II] deficit.

Another proposed explanation for the [C II]/FIR deficit is the increased absorption of ionizing UV photons by the dust in dust-bounded H II regions, which would result in increased FIR and decreased [C II] luminosity, respectively (Luhman et al. 2003). Abel et al. (2009) used radiative transfer models of the dust-bounded H II region to qualitatively reproduce the [C II]/FIR deficit trend. However, for the observed [C II]/FIR values in ALESS 49.1 and ALESS 57.1, the Abel et al. (2009) models require densities of $n \leqslant (1\text{–}2) \times 10^3\,{\rm cm}^{-3}$, i.e., much lower than those inferred from the PDR modeling. Furthermore, as already noted by Muñoz & Oh (2016), the dust drift time for high G_0, n values becomes very short compared to the lifetime of O/B stars. We follow Draine (2011) to estimate a dust drift time for a cluster of 10^3 O/B stars, providing an ionizing photon flux $Q_0 = 10^{52}\,{\rm s}^{-1}$. Given the density of $10^{3.5}$–$10^{4.0}\,{\rm cm}^{-3}$, the dust drift time becomes $t_{\rm drift} = (1.0\text{–}1.5) \times 10^5$ yr (Figure 9 of Draine 2011). Even if the H II regions in ALESS 49.1 and ALESS 57.1 are originally dust bounded, given the long duration of the starburst compared to $t_{\rm drift}$, we do not expect a significant fraction of them to be dust bounded at a given moment and hence do not expect the dust-bounded H II regions to dominate the [C II]/FIR deficit in ALESS 49.1 and ALESS 57.1.

5. Conclusions

We have investigated the morphology and kinematics of the [C II] 157.74 μm line emission and associated 160 μm rest-frame continuum in two $z \sim 3$ sources from the ALESS sample, based on the 0.″15 ALMA Band 8 imaging. The morphology and [C II] velocity field in both galaxies are consistent with an inclined rotating exponential disk. The [C II] rotation curves show a flattening within the inner 2–3 kpc radius, indicative of a potential dominated by a baryonic disk.

Comparing the resolved maps of the [C II] emission with those of CO (3–2) (Calistro Rivera et al. 2018), we found the [C II] surface brightness to be concentrated into a region a factor of 2–3 more compact than CO (3–2). In ALESS 49.1, we found evidence for a low surface brightness, extended ($R_{1/2} \sim 8$ kpc) [C II] component, accounting for up to 80% of the [C II] brightness. Based on mock ALMA observations, we excluded the possibility that [C II] and 160 μm continuum follow the same single-Gaussian surface brightness as the CO (3–2) emission.

We compared the [C II]/FIR and CO (3–2) observations to the PDRTOOLBOX PDR models (Kaufman et al. 2006; Pound & Wolfire 2008). These indicate intense FUV radiation field ($G_0 \sim 10^4$) and moderately high gas densities (n(H) = 10^4–$10^5\,{\rm cm}^{-3}$), comparable to the G_0 and n values found in the central regions of nearby starbursts (e.g., Contursi et al. 2002), as well as in other $z > 2$ SMGs (Stacey et al. 2010). We attribute the strong FUV field to massive star formation, rather than an obscured AGN.

We tested the applicability of the Stacey et al. (2010) technique for estimating FIR source size from unresolved [C II]/low-J CO/FIR observations to ALESS 49.1 and ALESS 57.1. The Stacey et al. (2010) method yields FIR sizes a factor of 2.5–3.5 more compact than measured from the u-v plane fitting; this bias causes the SFR surface density to be overestimated by up to 1 dex, having a potentially significant impact on the interpretation of low-resolution observations.

Both ALESS 49.1 and ALESS 57.1 show a pronounced [C II]/FIR deficit, with $L_{\rm [C\,II]}/L_{\rm FIR} = 10^{-4}$ to 10^{-3}. The resolved [C II]/FIR luminosity ratios fall below the empirical trend of Smith et al. (2017), indicating a change in physical conditions compared to the nearby star-forming galaxies. A comparison with PDR models indicated surface temperatures of 400–800 K; at such a high temperature, the occupancy of the upper fine-structure level of C^+ ions (and the [C II] luminosity) saturates, while FIR luminosity increases sharply. The most direct interpretation is that the strong [C II] deficit is a result of the C^+ fine-structure thermal saturation (Muñoz & Oh 2016). In addition, the resolved [C II]/FIR measurements in ALESS 49.1 and ALESS 57.1 scale with SFR surface density as $\Sigma_{\rm SFR}^{-0.53\pm0.12}$, in agreement with the thermal saturation scenario slope of –0.5 (Muñoz & Oh 2016). Although the photoelectric heating of the gas is reduced owing to positive grain charging, for the G_0, n values in ALESS 49.1 and ALESS 57.1 the thermal saturation is the main driving mechanism of the [C II]/FIR deficit. This contrasts with the local star-forming galaxies, which are found to have gas temperatures below the C^+ ionization energy (e.g., Díaz-Santos et al. 2017).

With only two galaxies in our sample, it is difficult to generalize our conclusions to the entire population of submillimeter galaxies. With ALMA now enabling routine observations of [C II] emission at redshift 3 and beyond, and with a rapid increase in the number of high-redshift sources with robust spectroscopic redshifts that are necessary for parallel [C II]/CO observations, this study is a precursor to future multitracer, resolved studies of ISM at high redshift and a necessary stepping stone to interpreting the [C II] observations at very high redshift.

The authors thank Frank Israel and Desika Narayanan for helpful discussions about the [C II]/CO extent.

This paper makes use of the following ALMA data: ADS/JAO. ALMA#2013.1.00470.S, #2015.1.00019.S, #2015.1.00948.S, and #2016.1.00754.S. ALMA is a partnership of ESO (representing its member states), NSF (USA), and NINS (Japan), together with NRC (Canada), MOST and ASIAA (Taiwan), and KASI (Republic of Korea), in cooperation with the Republic of Chile. The Joint ALMA Observatory is operated by ESO, AUI/NRAO, and NAOJ. M.R. and J.H. acknowledge support of the VIDI research program with project No. 639.042.611, which is (partly) financed by the Netherlands Organisation for Scientific Research (NWO). I.R.S. acknowledges support from the ERC Advanced Grant DUSTYGAL (321334) and STFC (ST/P000541/1). H.D. acknowledges financial support from the Spanish Ministry of Economy and Competitiveness (MINECO) under the 2014 Ramón y Cajal program MINECO RYC-2014-15686. J.L.W. acknowledges support from an STFC Ernest Rutherford Fellowship (ST/P004784/1).

Appendix A
Companion Sources in LESS 49 Field

Hodge et al. (2013) identified a nearby counterpart to ALESS 49.1–ALESS 49.2 (J2000 03:31:24.47–27°50′38.″1). Detected at the 4σ confidence level in 870 μm continuum ($S_{870\ \mu m} = 1.80 \pm 0.46$ mJy), it is included in the "main" ALESS sample. Additionally, ALESS 49.2 was detected in 3.3 mm continuum in ALMA Band 3 observations of Wardlow et al. (2018) with $S_{3.3\ mm} = 28 \pm 6\ \mu$Jy; however, Wardlow et al. (2018) do not detect any CO (3–2) emission from ALESS 49.2, suggesting that it is offset in redshift from ALESS 49.1. Finally, 1.4 GHz VLA observations (Biggs et al. 2011, based on Miller et al. 2008 data, ∼2 arcsec resolution) detect radio continuum emission from ALESS 49.2 at $\sim 4.5\sigma$ significance. The $\geqslant 4\sigma$ detections in these high-resolution observations confirm that ALESS 49.2 is a physical source, rather than an imaging artifact.

We do not find any significant Band 8 continuum or [C II] emission within a 1 arcsec radius of the position reported by Hodge et al. (2013). Given the small size of the ALMA Band 8 primary beam (FWHM = 14.″1) and the large distance of ALESS 49.2 from the phase-tracking center (∼9.″6), the emission from ALESS 49.2 will be attenuated by ∼70%. Therefore, we impose a 3σ upper limit of 1.2 mJy on the ALESS 49.2 620 μm continuum flux density. For a $z = 3$ source, this constraint is compatible with a modified blackbody SED with $T_{dust} \simeq 20$ K.

In addition to ALESS 49.2, Wardlow et al. (2018) detected significant 3.3 mm continuum emission from two additional sources in the vicinity of ALESS 49.1–ALESS 49.L and ALESS49.C. However, we do not detect any emission at $\geqslant 4\sigma$ significance in either Band 8 continuum or [C II] emission at the position of any of the Wardlow et al. (2018) sources. Accounting for the primary beam response, we put 3σ upper limits of $S_{620\ um} \leqslant 0.4$ mJy for both ALESS 49.L and ALESS 49.C. Given that ALESS 49.L and ALESS 49.C are detected at the $\sim 8\sigma$ level in the CO (3–2) and 3.3 mm continuum, respectively (Wardlow et al. 2018), we consider both sources to be physical. The companion sources in the LESS 49 field will be addressed in more detail using ALMA Band 4 observations in E. da Cunha et al. (2019, in preparation).

Appendix B
SED for ALESS 49.1 and ALESS 57.1

Figure 10 presents the best-fitting SEDs for ALESS 49.1 and ALESS 57.1, derived using the high-redshift version of MAGPhys (da Cunha et al. 2015). The UV-to-radio photometric data are taken from Swinbank et al. (2014) and supplemented by the new ALMA Band 3 (Wardlow et al. 2018), Band 4 (E. da Cunha et al. 2019, in preparation), and Band 8 (this work) continuum measurements.

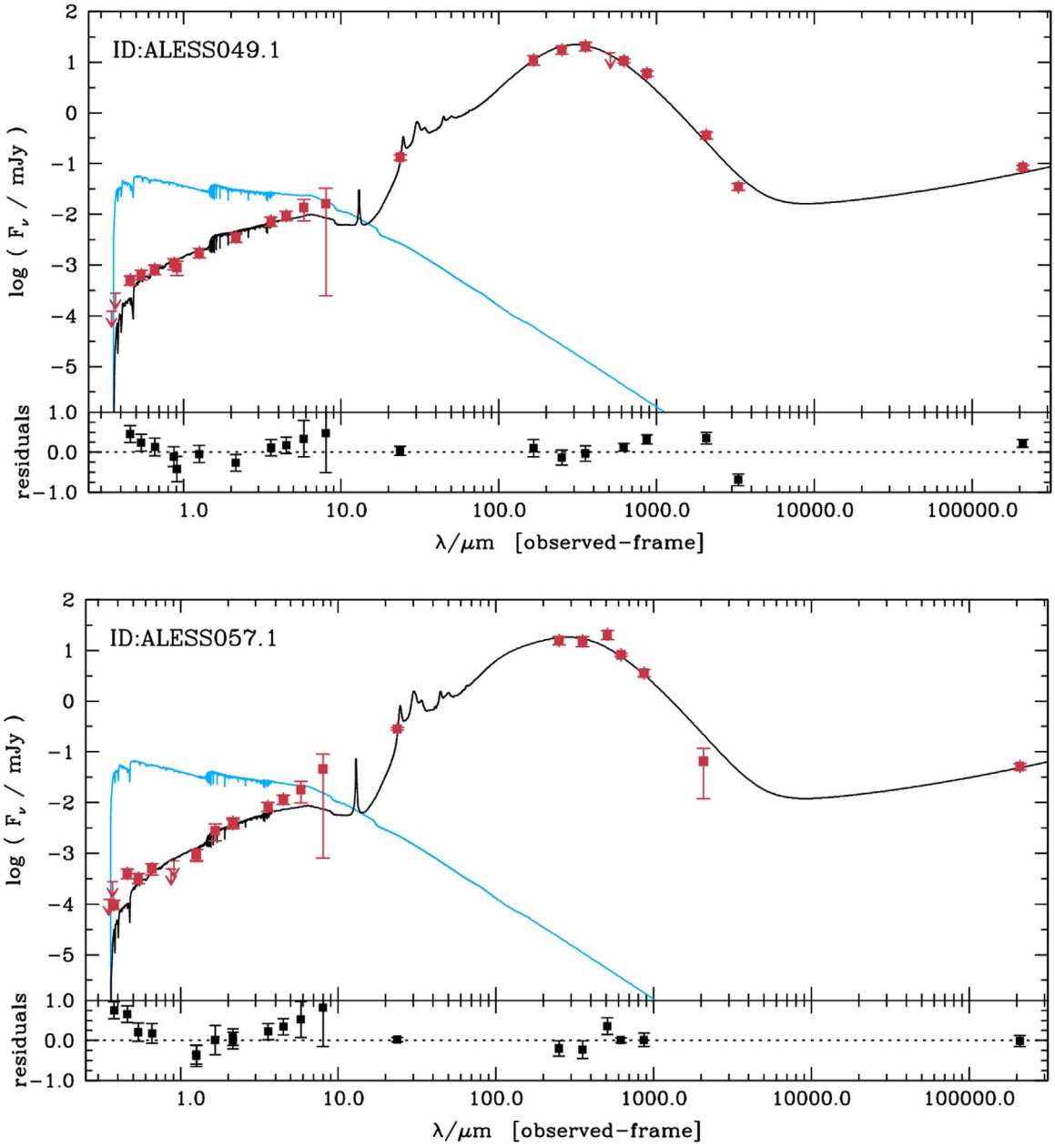

Figure 10. Multiwavelength photometry of ALESS 49.1 and ALESS 57.1, with best-fitting SED for ALESS 49.1 (left) and ALESS 57.1 (right) inferred from MAGPHYS modeling (black). The unattenuated stellar spectrum is shown in blue. The reduced χ^2 is $\leqslant 3$ for both sources.

ORCID iDs

Matus Rybak https://orcid.org/0000-0002-1383-0746
J. A. Hodge https://orcid.org/0000-0001-6586-8845
Ian Smail https://orcid.org/0000-0003-3037-257X
F. Walter https://orcid.org/0000-0003-4793-7880
P. van der Werf https://orcid.org/0000-0001-5434-5942
E. da Cunha https://orcid.org/0000-0001-9759-4797
Chian-Chou Chen https://orcid.org/0000-0002-3805-0789
H. Dannerbauer https://orcid.org/0000-0001-7147-3575
R. J. Ivison https://orcid.org/0000-0001-5118-1313
A. Karim https://orcid.org/0000-0002-8414-9579
J. M. Simpson https://orcid.org/0000-0002-8521-1995

References

Abel, N. P., Dudley, C., Fischer, J., Satyapal, S., & van Hoof, P. A. M. 2009, ApJ, 701, 1147
Alaghband-Zadeh, S., Chapman, S. C., Swinbank, A. M., et al. 2013, MNRAS, 435, 1493
ALMA Partnership, Vlahakis, C., Hunter, T. R., et al. 2015, ApJL, 808, L4
Armus, L., Mazzarella, J. M., Evans, A. S., et al. 2009, PASP, 121, 559
Bakes, E. L. O., & Tielens, A. G. G. M. 1994, ApJ, 427, 822
Bevington, P. R., & Robinson, D. K. 2003, Data Reduction and Error Analysis for the Physical Sciences (Boston, MA: McGraw-Hill)
Biggs, A. D., Ivison, R. J., Ibar, E., et al. 2011, MNRAS, 413, 2314
Bothwell, M. S., Smail, I., Chapman, S. C., et al. 2013, MNRAS, 429, 3047
Bouché, N., Carfantan, H., Schroetter, I., Michel- Dansac, L., & Contini, T. 2015, AJ, 150, 92

Brisbin, D., Ferkinhoff, C., Nikola, T., et al. 2015, ApJ, 799, 13
Calistro Rivera, G., Hodge, J. A., Smail, I., et al. 2018, ApJ, 863, 56
Carilli, C. L., & Walter, F. 2013, ARA&A, 51, 105
Carniani, S., Maiolino, R., Amorin, R., et al. 2017, MNRAS, 478, 1170
Casey, C. M., Narayanan, D., & Cooray, A. 2014, PhR, 541, 45
Chen, C.-C., Hodge, J. A., Smail, I., et al. 2017, ApJ, 846, 108
Cicone, C., Maiolino, R., Gallerani, S., et al. 2015, A&A, 574, A14
Contursi, A., Kaufman, M. J., Helou, G., et al. 2002, AJ, 124, 751
Cooke, E. A., Smail, I., Swinbank, A. M., et al. 2018, ApJ, 861, 100
Croxall, K. V., Smith, J. D., Pellegrini, E., et al. 2017, ApJ, 845, 96
da Cunha, E., Charlot, S., & Elbaz, D. 2008, MNRAS, 388, 1595
da Cunha, E., Groves, B., Walter, F., et al. 2013, ApJ, 766, 13
da Cunha, E., Walter, F., Smail, I. R., et al. 2015, ApJ, 806, 110
Danielson, A. L. R., Swinbank, A. M., Smail, I., et al. 2017, ApJ, 840, 78
de Blok, W. J. G., Walter, F., Smith, J.-D. T., et al. 2016, AJ, 152, 51
Decarli, R., Walter, F., Venemans, B. P., et al. 2018, ApJ, 854
Díaz-Santos, T., Armus, L., Charmandaris, V., et al. 2013, ApJ, 774, 68
Díaz-Santos, T., Armus, L., Charmandaris, V., et al. 2017, ApJ, 846, 32
Draine, B. T. 2011, ApJ, 732, 100
Dye, S., Furlanetto, C., Swinbank, A. M., et al. 2015, MNRAS, 452, 2258
Goldsmith, P. F., Langer, W. D., Pineda, J. L., & Velusamy, T. 2012, ApJS, 203
Graf, U. U., Simon, R., Stutzki, J., et al. 2012, A&A, 542, L16
Gullberg, B., De Breuck, C., Vieira, J. D., et al. 2015, MNRAS, 449, 2883
Gullberg, B., Swinbank, A. M., Smail, I., et al. 2018, ApJ, 859, 12
Herrera-Camus, R., Sturm, E., Graciá-Carpio, J., et al. 2018, ApJ, 861, 94
Hodge, J. A., Carilli, C. L., Walter, F., et al. 2012, ApJ, 760
Hodge, J. A., Karim, A., Smail, I., et al. 2013, ApJ, 768, 91
Hodge, J. A., Riechers, D., Decarli, R., et al. 2015, ApJL, 798, L18
Hodge, J. A., Swinbank, A. M., Simpson, J. M., et al. 2016, ApJ, 833, 103
Hollenbach, D. J., & Tielens, A. G. G. M. 1999, RvMP, 71, 173
Huynh, M. T., Emonts, B. H. C., Kimball, A. E., et al. 2017, MNRAS, 467, 1222
Huynh, M. T., Kimball, A. E., Norris, R. P., et al. 2014, MNRAS, 443, L54
Ivison, R. J., Papadopoulos, P. P., Smail, I., et al. 2011, MNRAS, 412, 1913
Ivison, R. J., Swinbank, A. M., Smail, I., et al. 2013, ApJ, 772, 137
Kaufman, M. J., Wolfire, M. G., & Hollenbach, D. J. 2006, ApJ, 644, 283
Kaufman, M. J., Wolfire, M. G., Hollenbach, D. J., & Luhman, M. L. 1999, ApJ, 527, 795
Lagache, G., Cousin, M., & Chatzikos, M. 2018, A&A, 609, A130
Lamarche, C., Verma, A., Vishwas, A., et al. 2018, ApJ, 867, 140
Langer, W. D., & Pineda, J. L. 2015, A&A, 580, A5
Litke, K. C., Marrone, D. P., Spilker, J. S., et al. 2019, ApJ, 870, 80
Luhman, M. L., Satyapal, S., Fischer, J., et al. 1998, ApJL, 504, L11
Luhman, M. L., Satyapal, S., Fischer, J., et al. 2003, ApJ, 594, 758
Madden, S. C., Geis, N., Genzel, R., et al. 1993, ApJ, 407, 579
Malhotra, S., Helou, G., Stacey, G., et al. 1997, ApJL, 491, L27
Malhotra, S., Kaufman, M. J., Hollenbach, D., et al. 2001, ApJ, 561, 766
McMullin, J. P., Waters, B., Schiebel, D., Young, W., & Golap, K. 2007, in ASP Conf. Ser. 376, Astronomical Data Analysis Software and Systems XVI, ed. R. A. Shaw, F. Hill, & D. J. Bell (San Francisco, CA: ASP), 127
Miller, N. A., Fomalont, E. B., Kellermann, K. I., et al. 2008, ApJS, 179, 114
Muñoz, J. A., & Oh, S. P. 2016, MNRAS, 463, 2085
Narayanan, D., & Krumholz, M. R. 2014, MNRAS, 442, 1411
Offringa, A. R., McKinley, B., Hurley-Walker, N., et al. 2014, MNRAS, 444, 606
Offringa, A. R., & Smirnov, O. 2017, MNRAS, 471, 301
Olsen, K. P., Greve, T. R., Narayanan, D., et al. 2015, ApJ, 814, 76
Oteo, I., Ivison, R. J., Dunne, L., et al. 2016, ApJ, 827, 34
Pineda, J. L., Langer, W. D., Velusamy, T., & Goldsmith, P. F. 2013, A&A, 554, A103
Planck Collaboration, Ade, P. A. R., Aghanim, N., et al. 2016, A&A, 594, A13
Pound, M. W., & Wolfire, M. G. 2008, in ASP Conf. Ser. 394, Astronomical Data Analysis Software and Systems XVII, ed. R. W. Argyle, P. S. Bunclark, & J. R. Lewis (San Francisco, CA: ASP), 654
Riechers, D. A., Hodge, J., Walter, F., Carilli, C. L., & Bertoldi, F. 2011, ApJL, 739, L31
Rybak, M., McKean, J. P., Vegetti, S., Andreani, P., & White, S. D. M. 2015a, MNRAS, 451, L40
Rybak, M., Vegetti, S., McKean, J. P., Andreani, P., & White, S. D. M. 2015b, MNRAS, 453, L26
Sandell, G., Mookerjea, B., Güsten, R., et al. 2015, A&A, 578, A41
Serjeant, S. 2012, MNRAS, 424, 2429
Smit, R., Bouwens, R. J., Carniani, S., et al. 2018, Natur, 553, 178
Smith, J. D. T., Croxall, K., Draine, B., et al. 2017, ApJ, 834, 5
Sofue, Y., Tutui, Y., Honma, M., et al. 1999, ApJ, 523, 136
Spilker, J. S., Aravena, M., Marrone, D. P., et al. 2015, ApJ, 811, 124
Stacey, G. J., Geis, N., Genzel, R., et al. 1991, ApJ, 373, 423
Stacey, G. J., Hailey-Dunsheath, S., Ferkinhoff, C., et al. 2010, ApJ, 724, 957
Stefan, I. I., Carilli, C. L., Wagg, J., et al. 2015, MNRAS, 451, 1713
Swinbank, A. M., Papadopoulos, P. P., Cox, P., et al. 2011, ApJ, 742, 11
Swinbank, A. M., Simpson, J. M., Smail, I., et al. 2014, MNRAS, 438, 1267
Tacconi, L. J., Genzel, R., Saintonge, A., et al. 2018, ApJ, 853, 179
Taylor, G. B., Carilli, C. L., & Perley, R. A. (ed.) 1999, in ASP Conf. Ser. 180, Synthesis Imaging in Radio Astronomy II (San Francisco, CA: ASP)
Tielens, A. G. G. M., & Hollenbach, D. 1985, ApJ, 291, 722
Vallini, L., Gallerani, S., Ferrara, A., Pallottini, A., & Yue, B. 2015, ApJ, 813, 36
Valtchanov, I., Virdee, J., Ivison, R. J., et al. 2011, MNRAS, 415, 3473
Walter, F., Carilli, C., Bertoldi, F., et al. 2004, ApJL, 615, L17
Walter, F., Riechers, D., Cox, P., et al. 2009, Natur, 457, 699
Wang, S. X., Brandt, W. N., Luo, B., et al. 2013, ApJ, 778, 179
Wardlow, J. L., Cooray, A., Osage, W., et al. 2017, ApJ, 837, 12
Wardlow, J. L., Simpson, J. M., Smail, I., et al. 2018, MNRAS, 479, 3879
Weiß, A., Kovács, A., Coppin, K., et al. 2009, ApJ, 707, 1201
Wolfire, M. G., McKee, C. F., Hollenbach, D., & Tielens, A. G. G. M. 2003, ApJ, 587, 278
Wolfire, M. G., Tielens, A. G. G. M., & Hollenbach, D. 1990, ApJ, 358, 116
Wright, E. L. 2006, PASP, 118, 1711
Zanella, A., Daddi, E., Magdis, G., et al. 2018, MNRAS, 481, 1976
Zhang, Z.-Y., Ivison, R. J., George, R. D., et al. 2018a, MNRAS, 481, 59
Zhang, Z.-Y., Romano, D., Ivison, R. J., Papadopoulos, P. P., & Matteucci, F. 2018b, Natur, 558, 260